Platy Pyroxene: New Insights into Spinifex Texture

Jack R. Lowrey[1], Tim J. Ivanic[2], Derek A. Wyman[1*] and
Malcolm P. Roberts[3]

[1]School of Geosciences, University of Sydney, Sydney, NSW 2006, Australia; [2]Geological Survey of Western Australia, Department of Mines and Petroleum, 100 Plain Street, East Perth, WA 6060, Australia; and [3]Centre for Microscopy, Characterisation and Analysis, University of Western Australia, Crawley, WA 6009, Australia

*Communicating Author

ABSTRACT

New evidence has emerged for a different type of platy spinifex texture that has not previously been documented in the existing literature, in this case from 2_8 Ga high-Mg basalts in the Murchison Domain of the Yilgarn Craton, where petrographic and geochemical evidence shows that the dominant platy mineral is pyroxene, rather than olivine. In our samples, two scales of plates are evident. Larger plates have lengths and widths that are approximately equal and range from ~1000 to 15 000 µm, with thicknesses typically ≲120 mm. These plates have [25 mm thick augite rims, and cores that are now a mixture of low-temperature hydrous alteration minerals. They occur in sets of similarly oriented crystals, and typically intersect other sets of crystals at oblique angles. A second population of smaller augite-only plates occur within the interstices of the larger plates; they have lengths and widths that range from 200 to 1500 µm, and thicknesses that are typically ≲50 µm. Pyroxene dendrites are also a typical component of this texture and represent a third scale of crystal growth, which probably crystallized shortly before the remaining liquid quenched to glass. All scales of pyroxene contained within this texture exhibit skeletal features and are considered to have crystallized rapidly. We discuss possible conditions that led to the crystallization of platy habits instead of the typical acicular ones. The exposed volcanic sequence in our study area is volcanologically similar to other Archean komatiites, such as those from the 2.7 Ga Abitibi greenstone belt, for example, and has probably experienced a similar cooling history; however, apart from having similar textures, we cannot demonstrate a komatiitic association. Liquid compositions, estimated from chilled flow margins, are distinctly lower in MgO (14_4–15_8wt %) and higher in SiO_2 (50.9 – 52.1 wt %) than those for most platy olivine spinifex-textured komatiites; from these compositions, we calculate dry liquidus temperatures of 1312–1342_C and mantle potential temperatures of 1440–1480°C. On the basis of these temperatures we question whether a mantle plume is a necessary element of their petrogenesis. 'Platy olivine spinifex' is an igneous texture that characterizes komatiites and its observation in outcrops or drill core (typically prior to, or in lieu of chemical analysis) leads geologists to classify a rock as a komatiite. Field descriptions may therefore drive assumptions and interpretations surrounding the prevailing tectonic or geodynamic setting at the time of emplacement. We emphasize the importance of careful discrimination between a variety of spinifex textures within a local volcanological framework and caution against the habit of making direct interpretations of rock type based on the existence of spinifex textures alone.

Key words: platy pyroxene; spinifex; Archean; dendrite; micro-tomography

INTRODUCTION

Spinifex textures are a striking feature of ultramafic to mafic rocks that are interpreted to form in lavas or high-level intrusions when crystals cool in the presence of a thermal gradient (Faure et al., 2006; Arndt et al., 2008). Individual crystals are typically olivine or pyroxene, which have plate-like or acicular aspect ratios and grow in situ in tightly clustered aggregates. When viewed in cross-section the texture has a superficially similar appearance to spinifex grasses (Trioda sp.), after which the texture was named (Nesbitt, 1971). Spinifex textures are largely restricted to Archean komatiites and komatiitic basalts, but they have also been identified in non-komatiitic suites, such as Cretaceous boninites (Wood, 1980), and in Proterozoic komatiitic basalts that are not always associated with komatiite sensu stricto (e.g. Arndt, 1982; Baragar & Scoates, 1987; Puchtel et al., 1996; Zhou et al., 2000).

The mineralogy of spinifex-textured rocks is rarely preserved in Archean terranes because their delicate skeletal features have typically been overprinted by repeated episodes of regional metamorphism, hydro-thermal alteration and surface weathering. More commonly the primary minerals are replaced by secondary minerals such as chlorite, serpentine, amphibole and talc. Many geologists who specialize in Archean granite–greenstone terranes use the heuristic rule that platy pseudomorphs indicate olivine precursors, whereas acicular pseudomorphs indicate pyroxene. A logical extension of this rule is to use platy spinifex textures to infer komatiitic affinity, because the bulk chemistry of an olivine spinifex rock has typically more than 18 wt % MgO and if it is assumed to be representative of the initial melt composition then the unit would be designated as komatiitic.

Here we define an important exception to these rules. In the Murchison Domain of the Youanmi Terrane, Yilgarn Craton, there are areas where the low-grade regional metamorphic regime (prehnite–pumpellyite to greenschist) has allowed for preservation of textures such as random acicular pyroxene spinifex, oriented acicular pyroxene spinifex ('string-beef'), and platy pyroxene spinifex. Table 1 includes a summary of spinifex or spinifex-like terminology that we have encountered in the literature, including at the crystal and crystal group scales. Platy pyroxene spinifex-textured rocks were initially described and mapped as 'komatiitic' because of their resemblance to platy olivine spinifex (Watkins & Hickman, 1990; Hallberg, 2000; Wyche et al., 2007; Van Kranendonk et al., 2013), but we show that non-cumulate rocks have compositions in the range of ~11–16 wt % MgO and 51–57 wt % SiO_2. These compositions are far less magnesian and more siliceous than typical olivine spinifex-textured rocks and, given the remarkable preservation of primary igneous textures, they were selected for detailed investigation of their unusual geochemistry. Platy pyroxene spinifex-textured rocks are abundant in our study area, and we suggest that they are a product of unusually high-Si and moderately high-Mg parental melts.

Considering the above findings, several localities worldwide probably require re-examination. We view our results as a first step towards clarification of moderate- to high-MgO volcanic rock classifications, particularly relevant to Archean and Proterozoic greenstone terranes.

GEOLOGICAL BACKGROUND

The chronostratigraphic and magmatic framework of the Murchison Domain has most recently been docu-mented by Van Kranendonk et al. (2013), who divided the supracrustal rocks of this area into three main strati-graphic groups: the Norie Group (2.825–2.800 Ga), Polelle Group (2.800–2.735 Ga) and Glen Group (2.735–2.710

Table 1. Summary of spinifex-related nomenclature.

Textural term/grouping	Dominant phase(s) identified	Description	Aspect ratio	Natural example reference
		Micro-scale texture		
Acicular/needly	Ca-Cpx or low-Ca Px, commonly chemically zoned	Crystals are elongate along the c-axis. Sections normal to c-axis are typically rhombic to euhedral. Characteristic of pyroxene in rapidly cooled high-Mg volcanics (e.g komatiitic basalt, boninite).	$L \gg W \approx T$	Canada (Arndt 1977); South Africa (Kareem and Bryerly 2003); Zimbabwe (Shimizu et al., 2005); Japan (Natland 1982); this study
Chain/lattice (Donaldson 1976) or swallowtail (Faure et al., 2003)	Olivine or pyroxene	Chain/lattice is used to describe dendritic forms with bladed or thinly tabular aspect ratios. The texture is named for their comprising numerous linked crystal units, which are typically H-shaped (in sections parallel to either [001] or [100]), and units are locally connected to one another by "tongues". Chains may grow in random or parallel orientation, (Donaldson, 1976).	$L \approx W \gg T$ or $L > W \gg T$	Zimbabwe (olivine and augite; Renner et al., 1994).
Plate/blade/tabular (collectively sheaves, plate sets)	Olivine or pyroxene (typically clinopyroxene)	Individual crystals may internally be solid, dendritic or skeletal.	$L \approx W \gg T$ or $L > W \gg T$	South Africa (Viljoen and Viljoen 1969); Australia (Nesbitt 1971); Canada (Arndt 1977); Zimbabwe; (Nisbet et al., 1987)
Plate, locally with acicular protruding terminations	Pyroxene (typically clinopyroxene)	Individual crystals may be solid or skeletal. Plates are typically discrete however, in some instances plates may develop acicular shaped protrusions at the crystal margins, which are elongate in the orientation of the crystallographic c-axis.	$L \approx W \gg T$	This study.
Dendritic (AKA arborescent)	Olivine, pyroxene, oxides	Branching crystals that are each made of several units in contrast to euhedral or skeletal crystals which are made of only one unit (Welsch et al., 2013). They form fractal or "hierarchical" (Fowler et al., 2002) crystal geometries. Many examples in volcanic and hydrothermal rocks. Associated with undercooling, and hence association with spherulites/varioles.	N/A	Canada (Fowler et al., 2002). Australia (Hallberg 2000); this study
		Macro-scale texture		
Harrisite	Olivine	Distinctive radiating bunches of >20 cm crystals, develops in layers within intrusive and some extrusive rocks, associated with olivine cumulates. The term 'harristitic texture' is typically used for a radiating, spinifex-like texture in intrusive rocks and is also applied to minerals other than olivine.		Scotland (Emeleus 1987 after Harker, 1908)

Ga). The study area extends from ~10 km SE of Meekatharra to ~25 km SSE of Meekatharra within the Polelle Syncline structure (Fig. 1). All the volcanic rocks that we describe from our study area belong to the Meekatharra Formation of the Polelle Group, which is dominated by high-Mg basalts, associated olivine–pyroxene cumulates and tholeiitic basalts.

In the Polelle Syncline (Locality 2; Fig. 1), the Lordy Basalt Member and Bassetts Volcanic Member are both predominantly fine-grained, vitrophyric, trachytic or porphyritic textured high-Mg basalts that typically contain abundant acicular pyroxene phenocrysts. Most flows are massive and undifferentiated, but some flows around the base of the Formation have differentiated into lower olivine–pyroxene cumulate layers and upper spinifex-textured flow tops. Watkins & Hickman (1990) and Hallberg (2000) described the Lordy Basalt Member as a high-Mg basalt, whereas Van Kranendonk et al.(2013) described it as a komatiitic basalt, with local komatiite horizons. The Bassetts Volcanic Member has recently been differentiated in the stratigraphy (from within the Lordy Basalt Member), on the basis of textural differences and boninite-like chemistry (Wyman & Kerrich, 2012). Overlying these high-Mg units is the Stockyard Basalt Member, which consists of fine-grained, massive or pillowed, tholeiitic basalt.

In the centre of the Polelle Syncline, at Locality 1 (Figs 1 and 2), the volcanic stratigraphy is dominated by high-Mg basalts of the Bundle Volcanic Member

(over-lying the Stockyard Basalt Member). Based on field textures that resemble platy olivine spinifex, these lavas have been described as komatiite (Hallberg, 2000; Wyche et al., 2007; Van Kranendonk et al., 2013) and high-Mg basalt (Watkins & Hickman, 1990). Locality 1 is the best-preserved sequence of spinifex-textured flows, which are described in greater detail in the 'Spinifex textures' section. Regional metamorphism, shearing deformation, granitic intrusion and dolerite dykes have affected portions of this sequence. Apart from a few distal granitic intrusions, all these are late in the geological history of the study area (i.e. post 2 73 Ga; e.g. Van Kranendonk et al., 2013) and the study area is located away from any pervasive overprinting events.

SAMPLE SELECTION AND ANALYTICAL PROCEDURES

Nineteen rock samples were collected from outcrops at Locality 1. The samples are representative of a continuous stratigraphic sequence, rich in high-Mg volcanic rocks. Most samples were collected from one transect that crosses the best exposed basal section of the sequence, and three samples were collected along-strike, at a slightly higher stratigraphic level (Fig. 2). Several samples were also collected from Locality 2, but these are described for petrography only, to com-pare the textures and crystal habits with those of samples from Locality 1. A comprehensive study of the geochemistry of samples from Locality 2 and the enveloping stratigraphy is in preparation. All rock samples were selected for low extents of metamorphism, alteration and veining, as well as their preservation of igneous textures. Effort was made to sample a broad range of bulk compositions.

X-ray computed tomography

A core of 7.5 mm diameter was drilled from a thin-section billet of an A_2 Zone platy pyroxene spinifex sample (209114). The core was scanned at 80 kV and 87 mA using an X-ray microscope (XRM) (Versa XRM520, Zeiss) running Scout and Scan software (v10.6.2005.12038, Zeiss). A total of 3201 projections were collected over 360°, each with a 5 s exposure; 2x binning and source filter LE5 were used to achieve a suitable signal-to-noise ratio and 0.4 x optical magnification was used to achieve an isotropic voxel resolution of 7 4 mm. Raw data were reconstructed using XMReconstructor software (v10.7.3679.13921, Zeiss) following a standard centre shift and beam hardening correction procedure. The standard 0.7 kernel size recon filter setting was also used. The visualization and analysis of data generated from the XRM scans was performed using AvizoVR software (v8.1.1, FEI).

The output of the scan is a map of the variation of the attenuation of X-rays as they are transmitted through the sample. The attenuation coefficient is linear and depends upon the average atomic number and density of the material through which the X-ray is trans-mitted. Where phases in a sample have contrasting density, or mean atomic number, they can typically be delineated and segmented using thresholding values of X-ray attenuation. In this instance, the attenuation coefficients from altered crystal cores overlap with those of altered matrix, and it was impossible to distinguish between these phases using automatic segmentation methods. Instead, a selection of crystals were segmented manually by selecting voxels belonging to an individual crystal using the AvizoVR segmentation editor.
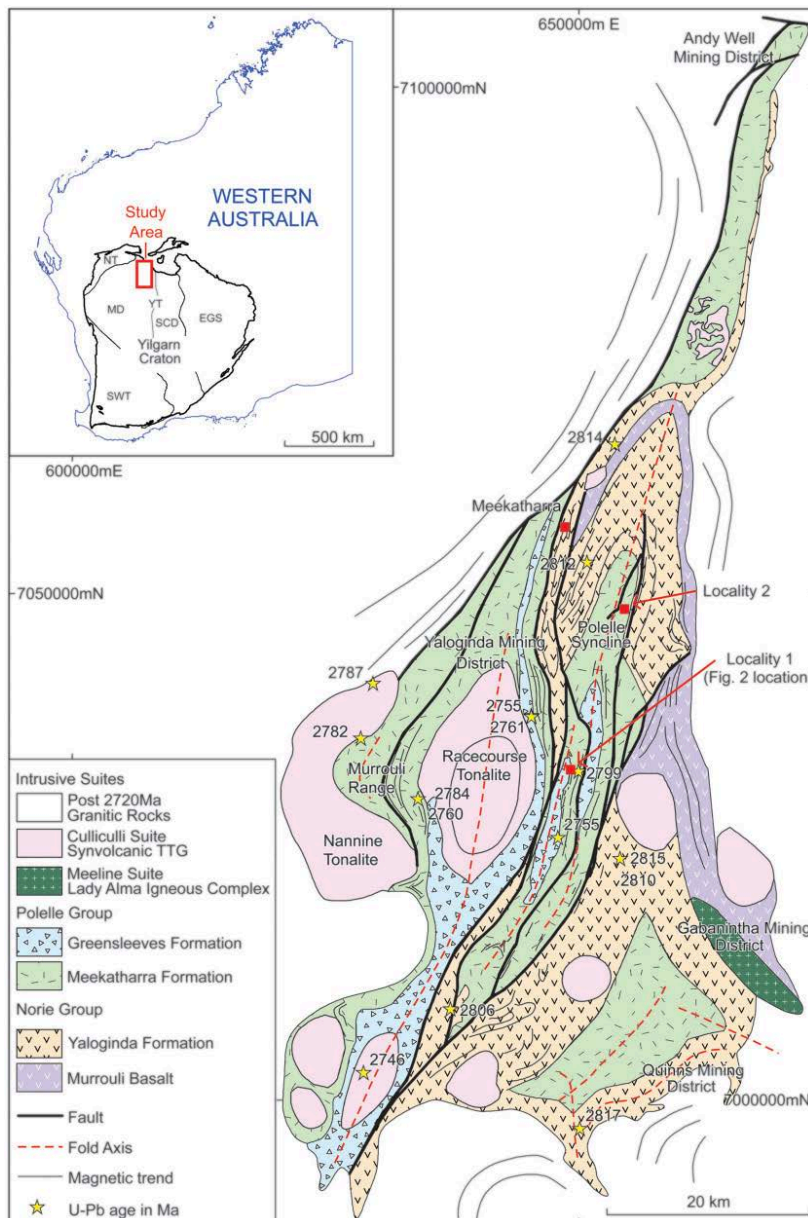
Fig. 1. Interpreted bedrock geology map of the northern Murchison Domain, Yilgarn Craton. This map shows the distribution of supracrustal groups and cogenetic intrusive suites, available geochronological data, major structural features and significant localities. Interpretation is based on 1:100 000 mapping by the Geological Survey of Western Australia (GSWA), and supplemented by our interpretation of aeromagnetic and Landsat multispectral images. Coordinates are relative to GDA94/MGA Z50. Inset abbreviations: MD, Murchison Domain; SCD, Southern Cross Domain; YT, Youanmi Terrane; NT, Narryer Terrane; SWT, South West Terrane; EGS, Eastern Goldfields Superterrane.

In several instances, the sample volume was less than the dimensions of larger crystals, and in these cases our measurements reflect their minimum dimensions. In other instances, where the entire crystal was contained within the volume, the measurements reflect their full dimensions. Table 2 records crystal dimension measurements.

Electron probe microanalysis and element mapping

Electron probe microanalysis (EPMA) was conducted on points within relict olivine, poikilitic pyroxene and Cr-spinel in B2 Zone cumulate sample 209122, as well as traverses across platy pyroxene crystals, dendritic pyroxene and Cr-spinel from A2 zone sample 209114. Average compositions are presented in Table 3 and individual point analyses are included in Supplementary Data Electronic Appendix 2 (supplementary data are available for downloading at http://www.petrology.oxfordjournals. org).

Polished thin sections (30 μm thickness) were analysed over the course of three analytical sessions using a JEOL 8530F electron microprobe equipped with five

tuneable wavelength dispersive (WD) spectrometers at the Centre for Microscopy, Characterisation and Analysis (CMCA) at the University of Western Australia. Elements were acquired using the following crystals: TAP for $SiK\alpha$, $AlK\alpha$, $NaK\alpha$ and $MgK\alpha$; PETJ for $CaK\alpha$ and $KK\alpha$; LIF for $FeK\alpha$, $NiK\alpha$ and $ZnK\alpha$; LIFH for $TiK\alpha$, $CrK\alpha$, $MnK\alpha$ and $VK\alpha$; which were analysed over 2–4 passes. Primary calibration of the electron microprobe was per-formed on well-characterized, homogeneous standards.

Operating conditions for point analyses were 40° take-off angle, accelerating voltage of 15 kV and beam intensity of 20 nA, with a fully focused beam. Element maps were acquired under the same conditions but with a beam intensity of 50 nA, pixel dwell time of 20 ms, a fully focused beam and a 1 μm x 1 lm pixel dimension. For point analyses, on-peak count times during session one for all elements ($SiK\alpha$, $TiK\alpha$, $AlK\alpha$, $CrK\alpha$, $FeK\alpha$, $NiK\alpha$, $MnK\alpha$, $MgK\alpha$, $CaK\alpha$, $NaK\alpha$, $KK\alpha$) were 20 s; during session two on-peak count times were 40 s for 11 elements ($SiK\alpha$, $TiK\alpha$, $ZnK\alpha$, $AlK\alpha$, $VK\alpha$, $CrK\alpha$, $FeK\alpha$, $NiK\alpha$, $MnK\alpha$, $MgK\alpha$, $CaK\alpha$), and 20 s for two elements ($NaK\alpha$, $KK\alpha$). For the element mapping session peak times for all 10 elements ($SiK\alpha$, $TiK\alpha$, $AlK\alpha$, $CrK\alpha$, $FeK\alpha$, $NiK\alpha$, $MgK\alpha$, $CaK\alpha$, $NaK\alpha$, $KK\alpha$) were 20 s.

EPMA point analyses were collected and post-processing was carried out using Probe for EPMA®. Elemental maps were acquired using a combination of Probe for EPMA® and Probe Image® with post-acquisition processing using CalcImage® and out put to Surfer® for further treatment. Unknown and standard intensities were corrected for deadtime. Matrix correction was by the Armstrong/Love Scott $\varphi(\rho z)$ method (Armstrong, 1988). Mean atomic number background corrections were used
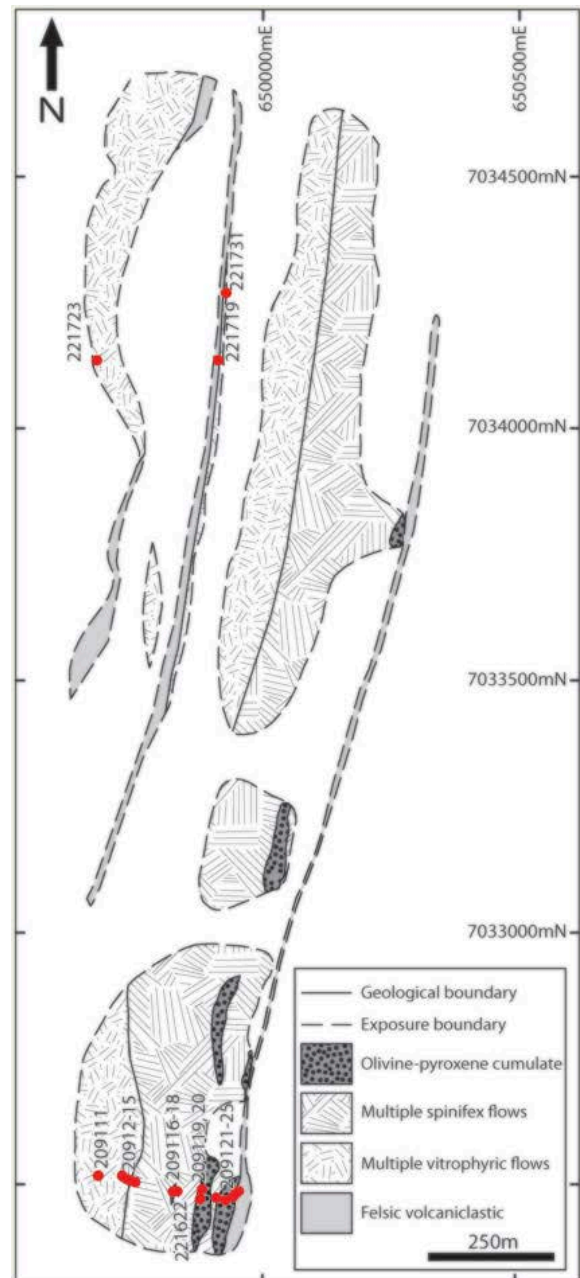

Fig. 2. Interpreted bedrock map of Locality 1 (see Fig. 1 for location). Outcrop is locally covered by saprolite. The dashed lines indicate areas with the most continuous outcrop. It should be noted that spinifex-textured basalt and vitrophyric-textured basalt map units both comprise many individual flows.

throughout (Donovan & Tingle, 1996). On-peak interference corrections were applied as appropriate (Donovan et al.,1993). Oxygen was calculated by cation stoichiometry. Results are presented in Table 3.

Whole-rock major and trace element compositions

Nineteen rock samples were sent to two laboratories for determination of major and

trace elements and loss on ignition (LOI). Well-characterized reference materials prepared by the Geological Survey of Western Australia, including a komatiitic olivine-cumulate (MW1) and a basalt (BB1), were submitted together with unknown samples. The major elements for both laboratories have a total uncertainty of ±1.5%. Total uncertainty for trace elements is ±10% in flow rocks and ±20% for olivine–pyroxene–Cr-spinel-orthocumulates.

Australian Laboratory Services
Thirteen samples were submitted to Australian Laboratory Services (ALS) in Wangara, Western Australia. A subsample of 200–1000 g was crushed in a jaw crusher to >70% passing 6 mm mesh and subsequently ground in a tungsten carbide ring mill to >85% passing 75 μm mesh.

Major and minor elements (Si, Ti, Al, Cr, Fe, Mn, Mg, Ca, Na, K, P) were analysed by mixing a 0.66 g aliquot of sample with lithium borate flux ($LiBO_2$, LiB_4O_7 and $LiNO_3$) in ~1:10 ratio, and then fusing the mixture at $1025^{O}C$ and pouring it into a platinum mould. The resulting disc was analysed by X-ray fluorescence spectrometry (XRF; their method ME-XRF26). LOI was determined by thermogravimetric analysis (their ME-GRA05). For resistive trace elements (Cr, V, Cs, Rb, Ba, Sr, Th, U, Nb, Zr, Hf, Y, La, Ce, Pr, Nd, Sm, Eu, Gd, Tb, Dy, Ho, Er, Tm, Yb and Lu), an aliquot of the sample was mixed with lithium borate and fused, then digested in acid and analysed by inductively coupled plasma mass spectroscopy (ICP-MS; their method ME-MS81). For base metals (Co, Cu, Ni, Sc and Zn) an aliquot of the sample was digested in a mixture of four acids ($HClO4$, $HNO3$, HF and HCl) and then analysed by inductively coupled plasma atomic emission spectroscopy (ICP-AES; their ME-4ACD81).

Intertek Genalysis
Six samples were submitted to Intertek Genalysis Laboratory Services Pty Ltd in Maddington, Western Australia. The methods were identical to those of ALS for sample preparation, analysis of major elements and LOI (their methods FB1, XRF and TGA). The methods were also the same for most trace elements (their methods FB6/4A, MS/OE) with the following exceptions. First, Cu, Cr, Ni, V and Zn were analysed by inductively coupled plasma optical emission spectroscopy (ICP-OES) rather than by ICP-MS. Second, Sc was digested using the fusion–mixed acid digest method, rather than the four-acid digest method, and was analysed by ICP-OES rather than ICP-MS.

Results for a subset of major and trace elements are presented in Table 4; these are recalculated to 100% on an anhydrous basis. The complete set of data is included in Supplementary Data Electronic Appendix 3

FIELD RELATIONS OF THE BUNDLE VOLCANIC MEMBER

The best-preserved spinifex-textured flows in the Polelle Syncline are at its centre, at Locality 1 (Figs 1 and 2; see also Locality 17 of Wyche et al., 2007); they crop out along a ridge composed of several low hills that extend along-strike for ~2500 m towards 010° from grid north (GDA94-MGA Z50). The width of the outcrop varies from 270 m at the southern limit to 700 m at the northern limit.

Surface exposure is better than in most of the Yilgarn Craton, estimated at 20–30%, but this still means that most of the sequence is interrupted by laterite. Contacts are obscured by saprolite and erosional debris in many places, and we note that erosionally recessive lithofacies may not be well represented by the exposed outcrop.

Sedimentary layering in the footwall rocks to the east of the (ultra-)mafic volcanic sequence dips at ~ 60 $^{\circ}$ towards the west, and sporadic exposures of inter-flow sedimentary horizons in the western part of the ultra-mafic sequence also dip towards the west. Based on an approximate dip of 60°, the volcanic sequence has an inferred true thickness 0230 m. Footwall sedimentary rocks have been dated using the sensitive high-resolution ion microprobe (SHRIMP) U–Pb in zircon method, which yielded an age of 2799 ± 2 Ma, which is interpreted to be the maximum age of deposition for the sedimentary footwall rocks and therefore also the maximum age for the overlying

Table 2. X-ray computed tomography 3D measurements of representative pyroxene crystals.

	Measurement number	Length μm (maximum dimension)	Width μm (max, 90° to length)	Thickness μm (mean, mode)	Rim thickness μm	Aspect ratio	Comment
1st order plates	1	1815	1115	120	15-20	L≈W≫T or L>W≫T	Plate intersects other 1st order plates
	2	>6965	2430	95	24		Plate's width is truncated by two other plates
	3	>1845	>1750	100	20-25		
1st order acicular crystals (associate with 1st order plates)	4	1330	160	140	20	L≫W≈T	
	5	1240	245	190	20-25		
	6	>1710	140	120	20		
2rd order plates (occur interstitial to 1st order plate sets)	7	1460	710	45	N/A	L≈W>T or L>W>T	
	8	770	480	55	N/A		
	9	275	230	50	N/A		
	10	240	165	70	N/A		
	11	192	101	30	N/A		
2nd Order acicular crystals	12	150	55	50	N/A	L>W≈T	Appear randomly oriented between oblique 1st order plate sets; limited by resolution of data
	13	430	50	50	N/A		
	14	730	50	50	N/A		

Note: > denotes a measurement where the crystal extrudes beyond the scanned volume in that dimension, and is thus a minimum measurement.

Table 3. Average mineral chemical compositions from EPMA point analyses

	1st order plate and needle cores (altered)*		1st order Plate cores (altered)		Plate rims (augite)		Acicular rims (augite)		Dendritic augite		Poikilitic augite		Poikilitic Opx		Olivine (Relict material)		Cr-spinel		Cr-spinel	
Sample	209114 (A2)		209114 (A2)		209114 (A2)		209114 (A2)		209114 (A2)		209122 (B2)		209122 (B2)		209122 (B2)		209114 (A2)		209122 (B2)	
	Calc. from Map Session		Session 1		Session 1		Session 1		Session 1		Session 2		Session 2		Session 2		Session 1		Session 2	
Point count	n=49555 pixels		n=55		n=18		n=28		n=7		n=12		n=19		n=10		n=35		n=10	
	Avg	SD	Avg	SD	Avg	SD	Avg	SD	Avg	SD	Avg	SD	Avg	SD	Avg	SD	Avg	SD	Avg	SD
SiO2	55.00	20.12	59.33	15.71	48.93	1.37	47.96	1.64	47.12	0.74	51.82	1.19	55.92	0.57	41.42	0.20	0.12	0.03	0.20	0.02
TiO2	0.20	0.76	0.13	0.29	0.84	0.18	0.93	0.22	1.06	0.20	0.47	0.13	0.11	0.02	0.02	0.01	0.40	0.04	0.38	0.01
Al2O3	8.10	4.60	5.92	4.41	7.37	2.46	7.53	1.55	8.67	0.59	3.39	1.07	0.99	0.25	0.06	0.01	9.48	0.36	8.80	0.24
Cr2O3	0.40	0.43	0.32	0.21	0.03	0.03	0.03	0.03	0.01	0.01	0.36	0.18	0.56	0.08	0.14	0.04	56.45	0.83	55.65	0.50
Fe2O3 (calculated)	-		-		0.31	1.31	0.60	2.15	0.00	0.77	1.19	0.96	0.00	0.59	0.00		5.79	0.39	6.01	0.25
FeO	9.80	4.84	9.43	3.96	10.77	0.39	11.19	0.49	13.96	0.35	4.90	0.62	7.39	0.63	10.53	0.49	13.80	1.40	17.46	2.02
NiO	0.20	0.29	0.03	0.04	0.02	0.02	0.02	0.02	0.01	0.01	0.10	0.01	0.15	0.01	0.39	0.01	0.13	0.02	0.16	0.01
MnO	Not analysed		0.16	0.07	0.23	0.05	0.23	0.08	0.27	0.04	0.18	0.02	0.19	0.01	0.18	0.01	0.18	0.06	0.27	0.01
MgO	14.30	6.24	14.41	5.22	13.68	2.11	13.32	1.58	12.07	0.91	18.42	1.36	32.77	0.34	48.20	0.31	12.34	0.98	9.62	1.34
CaO	2.50	2.96	5.33	4.64	16.49	1.98	16.95	1.74	15.15	1.23	18.29	1.44	1.53	0.21	0.18	0.01	0.07	0.03	0.06	0.02
Na2O	0.20	0.50	0.09	0.12	0.55	1.25	0.25	0.13	0.48	0.57	0.19	0.03	0.03	0.01	0.01	0.01	0.02	0.04	0.19	0.08
K2O	0.10	0.13	0.02	0.02	0.02	0.02	0.02	0.04	0.04	0.06	0.01	0.01	0.01	0.01	0.01	0.00	0.03	0.04	0.08	0.01
V2O3	Not analysed		Not analysed		Not analysed		Not analysed		Not analysed		0.07	0.01	0.03	0.01	0.02	0.00	Not analysed		0.16	0.01
ZnO	Not analysed		Not analysed		Not analysed		Not analysed		Not analysed		0.05	0.01	0.03	0.01	0.04	0.01	Not analysed		0.35	0.05
Total	90.80	9.75	95.17	4.40	99.22	0.60	99.01	0.54	98.84	0.37	99.42	0.45	99.71	0.57	101.20	0.27	98.80	0.53	99.39	0.42
Cation units					Cations per 6 oxygens												Cations per 4 oxygens			
Si	-		-		1.83	0.04	1.81	0.04	1.79	0.02	1.90	0.03	1.96	0.01	1.01	0.00	0.00	0.00	0.01	0.00
Ti	-		-		0.02	0.01	0.03	0.01	0.03	0.01	0.01	0.00	0.00	0.00	0.00	0.00	0.01	0.00	0.01	0.00
Al	-		-		0.32	0.10	0.34	0.07	0.39	0.03	0.15	0.05	0.04	0.01	0.00	0.00	0.37	0.01	0.35	0.01
Cr	-		-		0.00	0.00	0.00	0.00	0.00	0.00	0.01	0.01	0.02	0.00	0.00	0.00	1.47	0.02	1.48	0.01
Fe3+	-		-		0.34	0.04	0.02	0.07	0.01	0.02	0.03	0.03	0.04	0.02	0.00		0.14	0.01	0.15	0.01
Fe2+	-		-		0.01	0.01	0.35	0.01	0.43	0.01	0.15	0.02	0.18	0.02	0.21	0.01	0.38	0.04	0.49	0.06
Ni	-		-		0.00	0.00	0.00	0.00	0.00	0.00	0.00	0.00	0.00	0.00	0.01	0.00	0.00	0.00	0.00	0.00
Mn	-		-		0.01	0.00	0.01	0.00	0.01	0.00	0.01	0.00	0.01	0.00	0.00	0.00	0.01	0.00	0.01	0.00
Mg	-		-		0.76	0.12	0.75	0.08	0.68	0.05	1.01	0.07	1.71	0.02	1.75	0.01	0.61	0.04	0.48	0.06
Ca	-		-		0.66	0.08	0.69	0.07	0.62	0.05	0.72	0.06	0.06	0.01	0.00	0.00	0.00	0.00	0.00	0.00
Na	-		-		0.04	0.09	0.02	0.01	0.04	0.04	0.01	0.00	0.00	0.00	0.00	0.00	0.00	0.00	0.00	0.00
K	-		-		0.00	0.00	0.00	0.00	0.00	0.00	0.00	0.00	0.00	0.00	0.00	0.00	0.00	0.00	0.00	0.00
V	-		-		Not analysed		Not analysed		Not analysed		0.00	0.00	0.00	0.00	0.00	0.00	Not analysed		0.00	0.00
Zn	-		-		Not analysed		Not analysed		Not analysed		0.00	0.00	0.00	0.00	0.00	0.00	Not analysed		0.01	0.00
Total cation units	-		-		4.00		4.00		4.00		4.01	0.01	4.01	0.01	2.99	0.00	3.00	0.00	3.00	0.00
Wollastonite (Wo)	-		-		37.30	2.73	38.00	3.71	35.30	1.94	37.70	3.37	2.90	0.39	-		-		-	
Ferrosilite (Fs)	-		-		19.70	2.87	20.60	4.56	25.50	1.74	9.60	0.86	10.90	0.28	-		-		-	
Enstatite (En)	-		-		43.00	3.92	41.40	3.71	39.20	1.53	52.70	3.11	86.20	0.66	-		-		-	
Fosterite (Fo)	-		-		-		-		-		-		-		89.10	0.01	-		-	
Fayalite (Fa)	-		-		-		-		-		-		-		10.90	0.01	-		-	
Fe2+/(Mg2++Fe2+)	-		-		-		-		-		-		-		-		0.59	0.04	0.70	0.05
Fe3+/(Fe3++Cr+Al)	-		-		-		-		-		-		-		-		0.08	0.01	0.09	0.00
Cr/(Cr+Al)	-		-		-		-		-		-		-		-		0.89	0.00	0.89	0.00
Mg/(Mg+Fe2+)	-		-		0.69	0.05	0.68	0.06	0.61	0.02	0.87	0.01	0.91	0.00	0.89	0.00	0.41	0.04	0.30	0.05

* Average composition of pixels from all 1st order plate and needle cores in mapped area.

volcanic rocks in the study area (Wingate et al., 2008). The background sedimentary input is felsic or siliceous in composition and sediments were deposited as very fine grained sand-stones, locally turbiditic, which form the footwall and hanging wall, and occur sporadically as thin interflow horizons between the upper basalt flows. We interpret this to indicate a proximal to continental setting, or sub-aqueous intra-continental setting. The sedimentary rocks preserve rip-up marks and ripples, as well as graded bedding (Fig. 3a and b), which give a consistent younging direction towards the west (see also Wyche et al., 2007). This younging direction is corroborated independently by differentiated volcanic flow facies and geochemical trends (see below).

The easternmost (footwall) contact of the (ultra-)mafic sequence is abrupt and juxtaposes fine-grained olivine–pyroxene–Cr-spinel-orthocumulate against fine-grained siliceous volcanic-derived sediments. At Locality 1 this appears to be a conformable igneous contact (e.g. Fig. 3c), but the precise relationship (i.e. nature of thermal erosion, intermixing, etc.) cannot be further substantiated owing to talus material covering most of the contact.

flows, broadly comparable with komatiite sheetflow facies (e.g. Arndt et al., 2008), indicating a similar volcanic emplacement. The SE part of the mapped area is dominated by two ~30 m thick lenses of fine- to medium-grained serpentinized olivine–orthopyroxene–clinopyroxene–(Cr-spinel) orthocumulates. The two orthocumulates are both over-lain by ~5 m of pyroxene spinifex-textured rocks, which are interpreted to be flow tops; however, there are local breaks in the exposed outcrop. The extremities of the orthocumulates are largely obscured by in situ saprolite and so their boundaries are locally inferred on the out-crop map from in situ erosional lag and the positions of footwall or spinifex-textured rocks, which are less prone to erosion. Orthocumulate zones crop out less consistently along-strike, but always as discrete lens- or lozenge-shaped bodies, with similar orientations; they are consistently overlain by spinifex-textured rocks.

Above the two thicker flows there is an ~120 m sequence of thin (0.5–10 m) platy pyroxene spinifex and string-beef textured flows. We have identified only one thin (0.5–5 m) basal cumulate zone amongst these flows, which has been mostly eroded (Fig. 2); cumulate zones are either poorly

Table 4. Selected major, minor and trace element chemical analyses.

Sample ID	209111	209112	209113	209115	221731	221719	221723	209118	221722	209114	209117	209121	209116	209120	209122	209123	209124	209119	209125
Laboratory	ALS	Genalysis	ALS	ALS	Genalysis	Genalysis	Genalysis	Genalysis	Genalysis	ALS	ALS	ALS	ALS	ALS	ALS	ALS	ALS	ALS	ALS
Easting	649676	649727	649730	649748	649923	649908	649667	649828	649825	649739	649828	649906	649825	649878	649924	649938	649944	649874	649950
Northing	7032521	7032518	7032515	7032508	7034269	7034129	7034134	7032490	7032489	7032512	7032490	7032477	7032490	7032494	7032472	7032480	7032486	7032475	7032491
Field Description	Random acicular pyroxene spinifex SHMB			String-beef SHMB	Variolitic SHMB	Vitrophyric SHMB		A1 Zone Chilled Margin		A2 Zone platy spinifex			B2 Zone orthocumulate						Footwall sediment
SiO2_pct	53.28	57.54	54.56	52.43	54.52	61.25	53.62	49.29	50.79	55.86	51.54	52.1	44.5	44.43	43.85	43.98	43.82	43.79	75.07
TiO2_pct	0.69	0.69	0.75	0.62	0.84	0.99	0.67	0.6	0.6	0.64	0.62	0.65	0.27	0.3	0.28	0.32	0.29	0.28	0.31
Al2O3_pct	12.11	10.5	12.38	9.57	10.66	10.82	10.92	8.75	8.74	10.32	10.2	9.74	4.96	4.89	4.64	4.74	4.92	4.61	12.9
Cr2O3_pct	0.07	0.11	0.08	0.19	0.1	0.11	0.11	0.2	0.2	0.2	0.18	0.16	0.76	0.46	0.4	0.47	0.48	0.54	0.01
Fe2O3T_pct	12.05	8.7	9.9	10.64	12.28	9.22	10.36	11.04	11.18	10.29	10.66	10.14	9.93	10.39	9.86	10.48	10.54	10.53	1.75
MnO_pct	0.16	0.14	0.18	0.14	0.16	0.12	0.16	0.19	0.18	0.15	0.16	0.15	0.15	0.15	0.14	0.15	0.15	0.15	0.02
MgO_pct	9.28	8.5	8.5	14.15	9.75	5.64	11.33	15.35	13.99	11.05	13.9	14.3	29.8	29.4	30.1	29.2	29.2	30	0.56
CaO_pct	6.94	6.64	6.78	7.29	6.38	6.15	8.55	9.84	9.39	6.55	7.41	6.85	3.17	3.95	3.89	4.45	4.28	3.9	0.56
Na2O_pct	2.09	1.82	2.25	1.88	2.72	3.78	1.38	1.34	1.88	2.36	2.14	2.1	0.26	0.21	0.21	0.15	0.16	0.18	5.38
K2O_pct	0.23	0.73	1.02	0.09	0.49	0.14	0.46	0.2	0.48	0.2	0.36	0.34	0.06	0.06	0.07	0.08	0.07	0.06	2.34
P2O5_pct	0.07	0.102	0.08	0.06	0.068	0.068	0.067	0.057	0.059	0.06	0.06	0.07	0.03	0.03	0.03	0.04	0.03	0.03	0.09
LOI_pct	3.3	4.38	3.39	3.46	2.48	1.95	2.96	3.2	2.8	2.56	3.18	3.8	6.9	7.05	7.11	6.8	6.85	6.98	0.6
Total	100.33	99.89	99.93	100.54	100.47	99.88	100.60	100.07	100.309	100.26	100.45	100.44	100.8	101.33	100.59	100.87	100.8	101.06	99.88
Cr ppm	580	816	620	1290	691	746	756	1417	1393	1470	1380	1210	5480	3370	3010	3540	3690	3970	50
Ni ppm	135	175	160	362	171.7	203.7	178.6	318.1	346.3	230	243	237	1430	1380	1490	1290	1310	1380	18
Al2O3/TiO2	17.55	15.22	16.51	15.44	12.69	10.93	16.30	14.58	14.57	16.13	16.45	14.98	18.37	16.30	16.57	14.81	16.97	16.46	41.61
Mg-number	60.29	65.83	62.87	72.39	61.02	54.67	68.32	73.27	71.16	67.92	72.00	73.55	85.54	84.80	85.75	84.60	84.53	84.89	46.78

Differentiated flow sequence

Our outcrop mapping (Fig. 2) indicates that the hills at Locality 1 comprise many lava

developed in the case of thinner flows, or else they do not crop out. Individual flows can be traced for several tens of metres

along-strike, but owing to the many breaks in exposure we have mapped these flows collectively as a single unit (Fig. 2). Above the uppermost spinifex-textured flows, the textures change to vitrophyric or trachytic, with randomly oriented acicular phenocrysts of zoned pyroxene, varying in length from <1 to 5 cm, that are contained in a fine-grained or glassy matrix.

gradation of crystal morphology, size, and orientation. We use the classic komatiite nomenclature of Pyke et al. (1973) to describe their characteristics, from a basal cumulate B_2 Zone up through four non-cumulate zones, including, locally, a lower acicular pyroxene A_4 Zone, a spinifex-textured $A_{2–3}$ Zone and an upper chilled margin A_1 Zone. The following descriptions are mainly based upon thin-section observations, but also on hand-specimen examinations, SEM imagery and 3D X-ray computed tomography (CT) imagery.
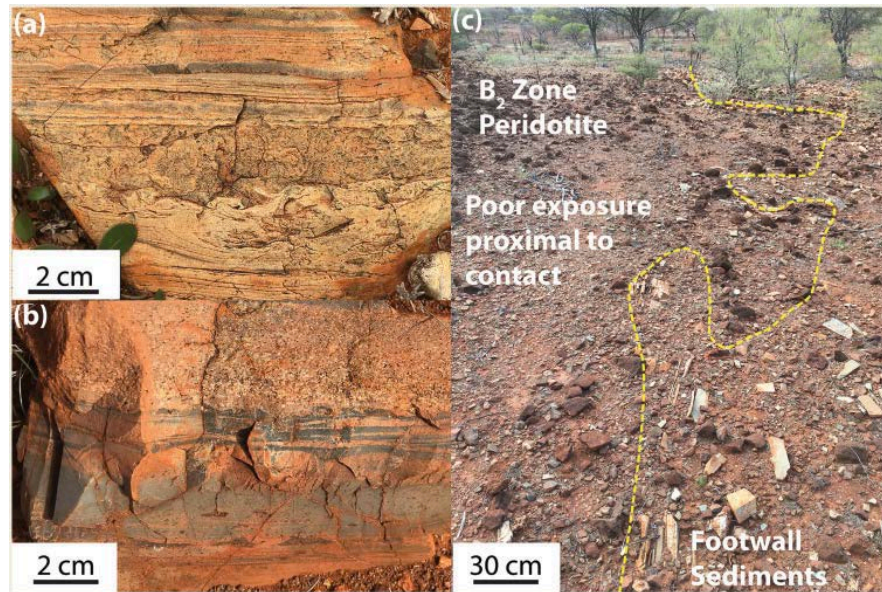
Fig. 3. Field photographs of Locality 1. (a) Scour marks and rip-up textures in footwall sediments indicate way-up towards the west (650204mE, 7034537mN GDA94/MGA Z50). (b) Graded bedding in interflow sediments indicates way-up towards the west (649940mE, 7034548mN GDA94/MGA Z50). (c) Footwall contact between peridotitic flow base and underlying sedimentary unit: the contact undulates along-strike, but the exact nature of the contact is frequently obscured by erosion and deposition of talus (649938mE, 7032480mN GDA94/MGA Z50).

A_1Zone—chilled flow top

The A_1 Zone has been observed in one outcrop (649828mE, 7032490mN GDA94/MGA Z-50), where it is interpreted to be the uppermost part of the flow, but owing to its fractured nature it is poorly preserved. In this example there is a thin (5–10 cm) break in expo-sure between the A_1 and A_2 Zones. This zone is pre-dominantly composed of devitrified glass, dendritic augite, and olivine phenocrysts with skeletal morphologies. Serpentinized, skeletal olivine pseudomorphs form [5% of the rock and typically have embayments containing matrix material (e.g. Fig. 5a). Most of the rock consists of fine-grained dendritic forms of augite and skeletal microphenocrysts that were probably olivine or pyroxene but are now entirely pseudomorphed by tremolite (e.g. Fig. 5b); these dendritic and skeletal crystals occur in a matrix of variably altered, devitrified glass. Locally within the A_1 Zone, Cr-spinel

PLATY PYROXENE SPINIFEX-TEXTURED FLOWS

Platy pyroxene spinifex occurs in all the high-Mg members of the Meekatharra Formation, but it is found in increasing abundance in order of Bassetts Volcanic Member < Lordy Basalt Member < Bundle Volcanic Member. In Figure 4 we show an ideal section through a typical platy pyroxene spinifex-textured flow from the Bundle Volcanic Member at Locality 1. Like platy olivine spinifex-textured flows (e.g. Munro Township), these flows are vertically differentiated into a spinifex-textured upper part and a cumulate textured lower part. They also exhibit similar vertical

crystals also have skeletal forms (e.g. Fig. 5c), which are not observed in the platy spinifex or cumulate zones and indicate that they crystallized more rapidly. We interpret these samples to be from chilled margins and representative of the liquid composition. Locally, the A_1 Zone contains sparse platy pyroxene crystals that are like those found in the A_2 Zone, but in the A_1 Zone they are not observed to be in contact with each other and they form ≲ 2% of the rock.

individual crystals range up to 15 mm in length and width, and 30–120 mm thick (see Table 2). Larger plates feature lozenge-shaped internal skeletal features (Figs 7c and 8a), and smaller plates have skeletal embayments along their margins (Fig. 8b), similar to those documented for diopside dendrites (e.g. Zhao et al., 2011). A third, finer dendritic form of pyroxene accommodates much of the interstitial volume between plates (e.g. Fig. 8c). In several flows the size of individual plates, and plate sets, coarsens downwards into

Flow Zone	Representative Samples	Ideal Section	Typical Petrographic Characteristics
A_1	209118, 221722		Chilled flow top; very fine grained with occasional skeletal olivine phenocrysts and plates of pyroxene; cruciform shaped chromium spinel, and abundant skeletal microphenocryst pseudomorphs (after olivine or pyroxene)
A_2	209114, 209117, 209121		Random spinifex textured zone; sets of sub-parallel plates intersecting one another at seemingly random, oblique angles; locally flows exhibit a gradational transition from fine to coarse plates downwards through the profile.
A_3			Locally there is a gradational transition from the A_2 Zone into an A_3 Zone where all plate sets are oriented almost perpendicular to the flow top; in these instances the plates form cone shaped clusters that fan out towards the bottom of the flow. Dominant plate sets, which are interpreted to have crystallized first, truncate subordinate sets. Plate growth terminates abruptly at the interface with the underlying A_4 zone.
A_4			A layer of tightly packed zoned-pyroxene crystals that mostly have acicular morphologies, but with some platy crystals. Platy crystals are finer than acicular crystals, and all crystals in this layer are oriented randomly. Matrix material is very fine grained and strongly altered.
			No preserved contacts between A Zone and B Zone in outcrop
B_2	209116, 209119, 209120, 209122, 209124		Predominantly equant olivine and poikilitic pyroxene, but also occasional equant pyroxene. Abundant equant euhedral chromite. Matrix comprises predominantly fibrous textured, intergrown crystals of plagioclase and Ca-rich clinopyroxene.
			Chilled flow base

Outcrop preserving contact relationships between A_2, A_3, and A_4 Zones

Fig. 4. Spinifex zone terminology applied to a generalized flow sequence from Locality 1, with petrographic notes. Inset showing a platy spinifex horizon with preserved contacts between the A2, A3 and A4 Zones (649896mE, 7032746mN GDA94/MGA Z50). Vertical scale is approximately 0_5–2 m. Sample IDs are indicative of relative position within their respective flows only. The samples were collected from several different flows and their locations are shown in Fig. 2.

A2–3 Zone—platy pyroxene spinifex

The A_2 'random' platy pyroxene horizon consists of thin plates of pyroxene that are typically arranged in sets of several crystals with similar orientations (Fig. 6). Plate sets intersect one another obliquely (e.g. Figs 7a, b and 8), giving the impression of an overall random orientation. In the upper parts of platy textured spinifex zones,

the flow.

Orthogonally cut surfaces of hand specimens show that most plates are well formed and continuous, but in thin section the edges of plates locally have acicular protrusions, continuing in the plane of the plate. This is also observable in the X-ray CT imagery. Where thin sections intersect aligned acicular pyroxene crystals, they are in crystallographic continuity with one
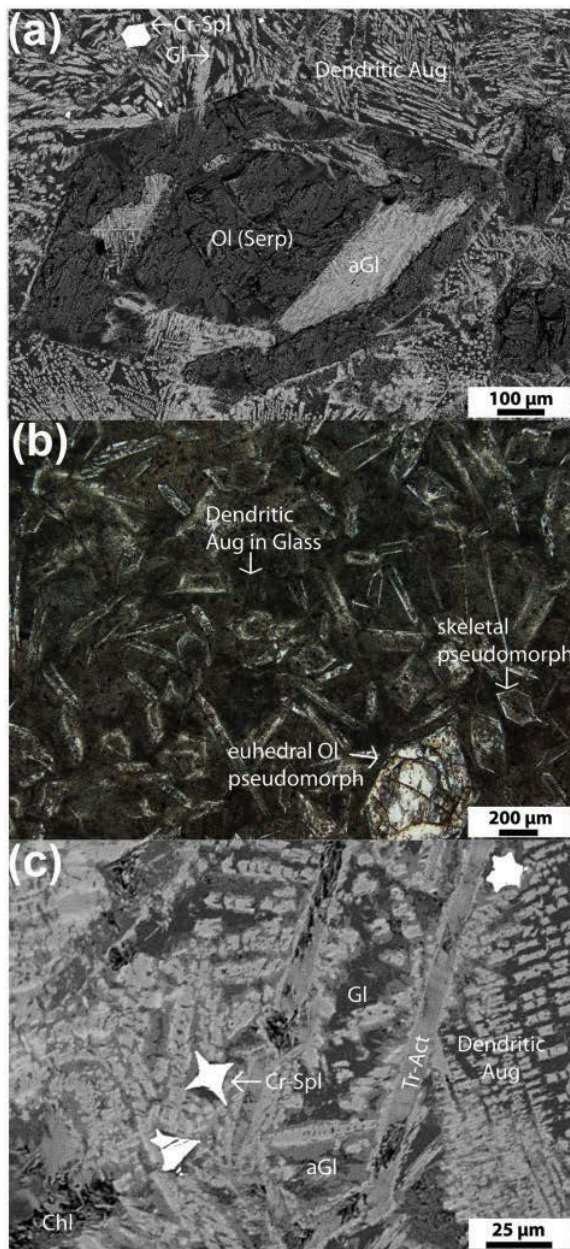
Fig. 5. Images of A1 Zone chilled flow top (sample 209118). (a) Back-scattered electron (BSE) image showing large skeletal serpentinized olivine pseudomorph [Ol-(Serp)] in a dendritic augite] (Aug) and devitrified glass (Gl) matrix, which is locally altered (aGl). The open and enclosed embayments filled with matrix material should be noted. (b) Photomicrograph in plane-polarized light (PPL) showing tremolite pseudomorphing skeletal olivine or pyroxene and euhedral olivine pseudomorph in a glassy matrix. (c) BSE image of skeletal cruciform-shaped Cr-spinel (Cr-Spl) crystals (white) in matrix of dendritic pyroxene and locally altered glass (aGl) matrix. Silicate phenocrysts have been altered largely to tremolite–actinolite (Tr-Act) and chlorite (Chl).

another, and with adjacent plates. Plates within a set are also typically in near crystallographic continuity, as observed by their similar extinctions in cross-polarized light. Locally, acicular crystals that stack side-by-side appear to merge along their length to form a composite crystal (e.g. Figs 8e and 9a); this is discussed in more detail in the 'X-ray computed tomography' section. Interstitial dendritic augite also has preferred orientations and platy morphologies, similarly to the larger, zoned pyroxene plates (e.g. Fig. 9b).

Invariably, the cores of larger plates consist of low-temperature hydrous alteration minerals, mostly chlorite, and are mantled by a 10–30 μm rim of augite (e.g. Fig. 7c), like zoned pyroxene phenocrysts in the random acicular pyroxene spinifex and string-beef textured examples. In the underlying Lordy Basalt Member, acicular pyroxene phenocrysts retain variably preserved augite cores, whereas in the Bassetts Volcanic Member zoned pyroxene phenocrysts have augite rims but retain variably preserved pigeonite cores, and by analogy we suggest that plate cores were also originally augite or pigeonite (see 'Mineral chemistry' section).

Although euhedral olivine is found only in the cumulate B_2 Zone, locally within the A_2 Zone there are skeletal olivine pseudomorphs (e.g. Fig. 10), which demonstrate that olivine was also a liquidus phase. Olivine phenocrysts that were not trapped between larger pyroxene plates probably settled downwards whilst continuing to crystallize into polyhedral forms; this is supported by similar FeO/MgO ratios in polyhedral olivine phenocrysts in B_2 Zone sample 209122, compared with the estimated liquid composition derived from A_1 Zone chilled margins (see 'Whole-rock major and trace element compositions').

As with the olivine spinifex A_{2-3} Zone, random platy pyroxene of the A_2 Zone grades downwards into 'oriented' platy pyroxene of the A_3 Zone. The A_3 oriented

platy pyroxene horizon was observed in two outcrops (649896mE, 7032746mN & 649754mE, 7032527mN, GDA94/MGA Z-50). In a profile section through (i.e. x–z or y–z section) both flows there is a gradational change from plate sets with a random orientation (i.e. A_2 Zone), down into sets where individual plates are all consistently oriented near-vertical (i.e. A_3 Zone). These subvertical plate sets spread out towards the bottom of the flow (Fig. 11a), yielding an overall steep-sided conical- or pyramid-like structure. In a section through the A_3 Zone, perpendicular to the vertical profile (i.e. x–y section), plate sets intersect one another at oblique angles relative to adjacent plate sets (Fig. 11b), similarly to plate sets in a section at any angle through the A_2 Zone 'random' platy spinifex.

Fig. 6. Field photograph of A2 Zone platy pyroxene spinifex at Locality 2 (655631mE, 7051848mN GDA94/MGA Z50; Fig. 1). Coarse obliquely intersecting plate sets should be noted; hence the descriptor 'random' spinifex. Individual plates measure up to 1 5 cm.

A_4 Zone—randomly oriented acicular pyroxene

The A_4 Zone has been identified at one outcrop at Locality 1. In this instance, it is composed predominantly of acicular pyroxene phenocrysts and sparse randomly oriented, fine-grained platy pyroxene pseudomorphs like those in the $A_{2–3}$ Zone (Fig. 12). This zone is similar to the zone of acicular pyroxene phenocrysts reported by Arndt et al. (2008, fig. 2.23d) in a position below the A3 Zone at the Proterozoic komatiitic basalt locality of Gilmour Island in Canada.

B_2 Zone—orthocumulate

A commonly documented feature in platy olivine spinifex-textured flows is the occurrence of horizontally aligned skeletal olivine between the A_3 Zone and the B_2 Zone (e.g. Arndt, 1986; Renner et al., 1994; Kerr et al., 1996), where it is typically referred to as the B1 Zone; we do not observe any occurrences of this horizon in our study area. However, in keeping with the terminology used widely for spinifex-textured flows, we use the term 'B_2 Zone' for all cumulate-facies rocks in the mapped area (Fig. 2). All examples of cumulate-facies rocks that we observed in outcrop were similar in terms of their grain size and mineralogy; all samples were homogeneous in their petrography and chemistry. The B_2 Zone is the most continuous and best-preserved horizon within the sequence. Olivine is a cumulus phase, and forms polyhedral equant phenocrysts that are now mostly serpentinized, but local unaltered relics remain (e.g. Fig. 13a). Olivine crystals frequently contain inclusions of euhedral, equant Cr-spinel and melt inclusions (Fig. 13b and c). Cr-spinel also occurs as phenocrysts in the interstices between olivine phenocrysts. Orthopyroxene and augite typically form large oikocrysts, which partially or fully overgrow smaller olivine and Cr-spinel chadacrysts; these pyroxenes remain mostly unaltered. Orthopyroxene is also locally present as a cumulus phase, but these are typically serpentinized. Locally, orthopyroxene and augite form coarsely

branching textures (Fig. 13d), loosely resembling but coarser than typical plate dimensions at Locality 1.

Similar crystal morphologies have been recognized in fractionated gabbroic layers below A_{2-3} Zone in komatiite flows in the Archean Abitibi Greenstone Belt (Arndt, 1977). Plagioclase and augite have crystallized as fibrous intergrowths in domains of residual liquid.

ACICULAR PYROXENE HABITS

Random acicular pyroxene spinifex

At Localities 1 and 2 (Fig. 1) there are excellent examples of basaltic flows that contain abundant acicular pyroxene phenocrysts (Table 1; see also 'vitrophyric basalts' in Fig. 2). Their micro- to macro-

scale features are comparable with those of many Archean and Proterozoic komatiitic basalt sequences (e.g. Arndt et al., 1977, 2008; Shimizu et al., 2005), Phanerozoic boninites (e.g. Wood, 1980; Natland, 1982; Bloomer & Hawkins, 1987; Taylor et al., 1994), and even quartz-normative lunar basalts (e.g. Lofgren et al., 1975). Most of these needle-textured horizons are characterized by abundant, randomly oriented, acicular pyroxene phenocrysts set in a fine-grained matrix of devitrified glass or intergrown fibrous or plumose augite and plagioclase. An example of this texture in a hand sample from Locality 1 is shown in Fig. 14a. In this example, phenocrysts range between <0.5 and 2 cm, but throughout the study area there are locally megacrysts up to 10 cm. Pyroxene phenocrysts are typically compositionally zoned with augite rims and pigeonite cores; most examples are now chlorite, but some retain unaltered pigeonite. In these instances the rims and cores are not in crystallographic continuity. Pigeonite cores and augite rims are themselves also internally chemically zoned, becoming increasingly Fe–Al rich and Mg-poor

outwards towards the crystal edge. Many of the phenocrysts exhibit simple twinning, and occasionally form cruciform-shaped phenocrysts (Fig. 14b and c).

'String-beef' (oriented pyroxene spinifex)

A variation of acicular pyroxene spinifex is known as 'string-beef' texture, documented first in Canada by Arndt et al. (1977). This is composed almost entirely of tight clusters of acicular-shaped pyroxene phenocrysts,
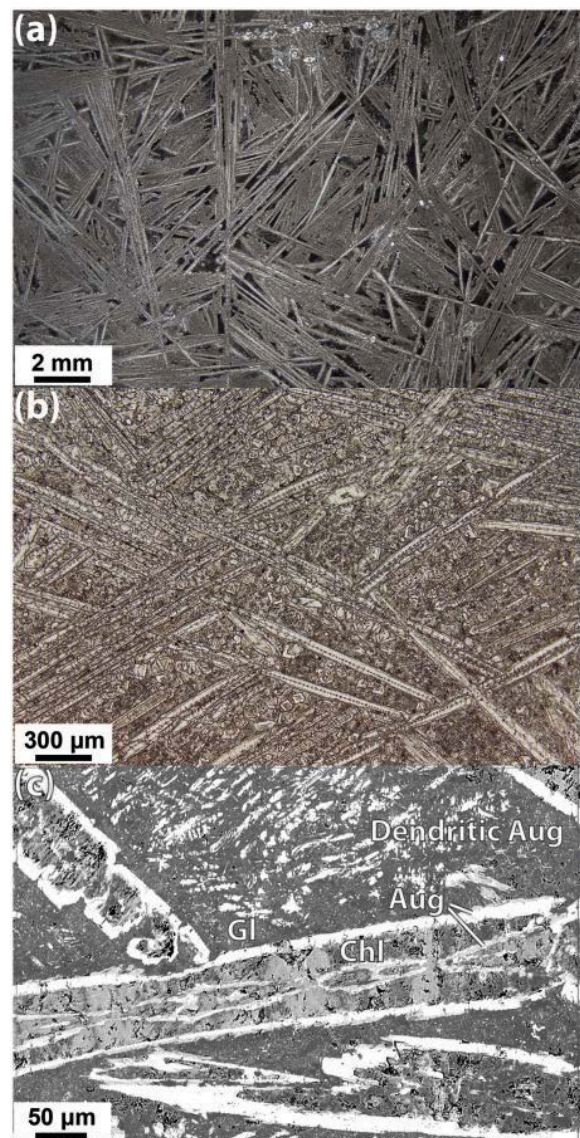
Fig. 7. Images of A2 Zone random platy pyroxene spinifex (sample 209114). (a) Thin section in PPL (larger field of view). (b) The same thin section in PPL (smaller field of view). The spaced internal texture in the cores of the plates should be noted. (c) BSE image of A2 Zone pyroxene plates showing lozenge- shaped internal structures similar to those described for dendrites (e.g. Zhao et al., 2011).

with little or no matrix material. At Locality 1 there are well-preserved, [5 m thick horizons of string-beef textured basalts (e.g. Fig. 15a).

DENDRITIC PYROXENE HABITS

Dendritic textures are locally preserved at Localities 1 and 2 in platy pyroxene spinifex and vitrophyric textured basalts. In the platy pyroxene spinifex samples, dendritic pyroxene typically occupies the interstitial spaces between plate sets and is surrounded by altered, devitrified glass. Dendritic pyroxene superficially resembles platy pyroxene

Fig. 8. BSE image of A2 Zone pyroxene crystals (sample 209114) highlighting: (a) rhombus/lozenge- and hourglass-shaped skeletal features in first-order plate; (b) skeletal second-order augite plate; (c) dendritic pyroxene accommodating interstices; (d) section through a series of acicular pyroxene crystals perpendicular to a first-order plate set; (e) section through stacked/merged acicular crystals, transitional to plate and similar to observations for platy olivine (Faure et al., 2006; Fig. 5).BSE image of A2 Zone pyroxene crystals (sample 209114) highlighting: (a) rhombus/lozenge- and hourglass-shaped skeletal features in first-order plate; (b) skeletal second-order augite plate; (c) dendritic pyroxene accommodating interstices; (d) section through a series of acicular pyroxene crystals perpendicular to a first-order plate set; (e) section through stacked/merged acicular crystals, transitional to plate and similar to observations for platy olivine (Faure et al., 2006; Fig. 5).

Individual pyroxene crystals are typically <500 mm in diameter and 05 cm long (Fig. 15b). Locally, there are examples where the phenocrysts are less densely clustered, and phenocrysts branch or fan out from a central nucleus (e.g. Fig. 15c). On the outcrop scale this tendency to branch and fan out can form conical structures that are 10–50 cm in height (e.g. Fig. 15d), similar to those described for the Witkop Formation in the Nondweni Greenstone Belt (Wilson & Versfeld, 1994). In that example, Wilson & Versfeld suggested that the cone structures give a reliable way-up direction; pyroxene crystals branch out and grow away from the chilled margin into the liquid below.

crystals, but at a finer scale (e.g. Fig. 16a). The dendrites have similar X-ray intensities to augite plate rims, and smaller augite-only plates (see 'X-ray computed tomography'), and EPMA indicates that they have similar compositions. In vitrophyric textured samples (221629 and 221701) dendrites are also surrounded by devitrified glass and are similarly represented by several orders of scale (<5 mm to 30 mm wide). However, in these cases dendrites have complicated geometries that include central chains that vary between straight and curved, and bifurcations that are typically at right angles to the central chain (e.g. Fig. 16b). In our samples, the dendritic pyroxene appears to

have crystallized in the interstices between plates and needles prior to the remaining liquid quenching to glass.
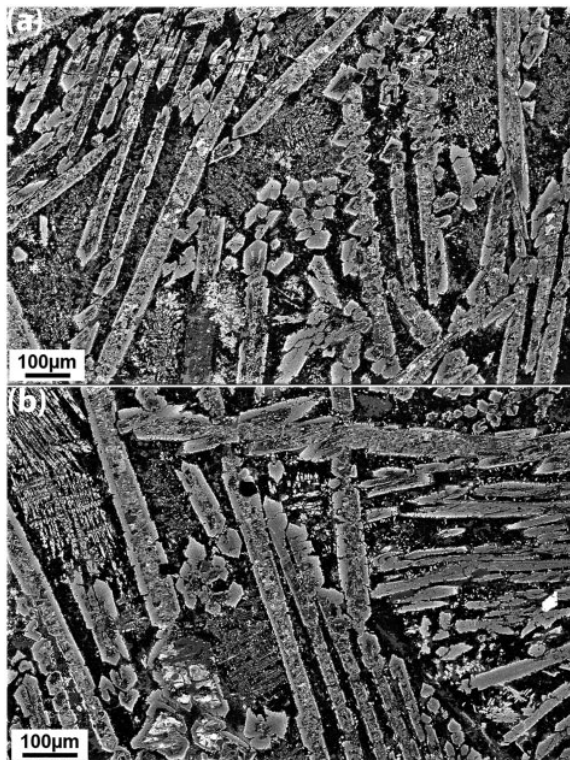
Fig. 9. BSE images of A$_2$ Zone pyroxene plates (sample 221628 from Lordy Basalt Member from Locality 2; see Fig. 1). (a)Locally, plates show a transition into acicular crystals that are joined along (100) crystal faces, and outer rims of both plates and acicular crystals have a higher X-ray intensity in BSE image; (b) weakly zoned core material near the unaltered rims; it is possible that this is representative of all core material, or that the more heavily chloritized parts were originally more magnesian (i.e. Mg-orthopyroxene, pigeonite or amphibole; see 'Mineral chemistry' section), and were altered to chlorite +SiO$_2$. In the upper left corner of the image, dendritic augite mimics the growth of adjacent plates, but on a smaller scale.

X-RAY COMPUTED TOMOGRAPHY

To address concerns over whether the pyroxenes were truly platy, rather than being aggregates of parallel-oriented acicular crystals, we performed an X-ray computed tomography (X-ray CT) scan of a small cylindrical subsample of sample 209114. We have included videos to allow a 3D view of the whole volume analysed (see Supplementary Data Electronic Appendix 1).
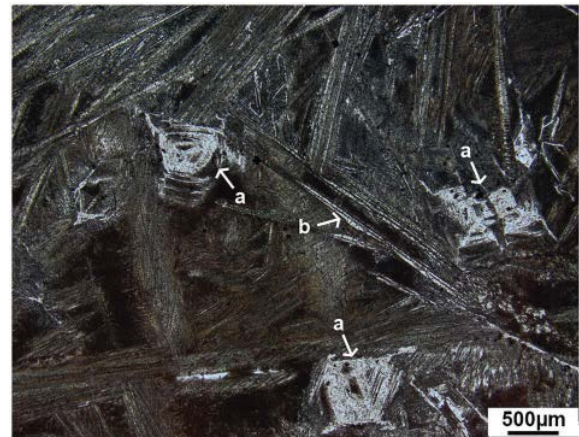
Fig. 10. Photomicrograph of A2 Zone sample 209117 (PPL)highlighting (a) skeletal olivine pseudomorphs and (b) thinplates of pyroxene forming sets in the matrix.

Representative plates were traced within the sample using the manual segmentation tool within Avizo®: examples of these segmented plates are illustrated in Fig. 17a and their measurements are reported in Table 1. Cr-spinel occurs throughout the volume, easily recognized by its high linear attenuation coefficient values (high X-ray intensity values); crystals are typically euhedral and range from 15 to 80 mm in diameter. Material interstitial to pyroxene and spinel crystals is altered devitrified glass. Pyroxene crystals can be divided into two broad categories: those with a thickness of ≳95 mm, which contain an altered core component (first order), and those with a thickness ≲70 mm, which do not contain an altered core (second order).

For larger (first-order) plates (>500 μm length and/or width) sections spaced at 25 μm were digitized and then the intervals between were interpolated; the resulting volume was inspected on each interpolated section to ensure that it honours the plate boundaries. For smaller (second-order) plates (<500 μm length and/or width every section was digitized manually. First-order plates intersect one another at oblique angles (e.g. Fig. 17b), but in some instances they are only partially truncated by one another and continue beyond the
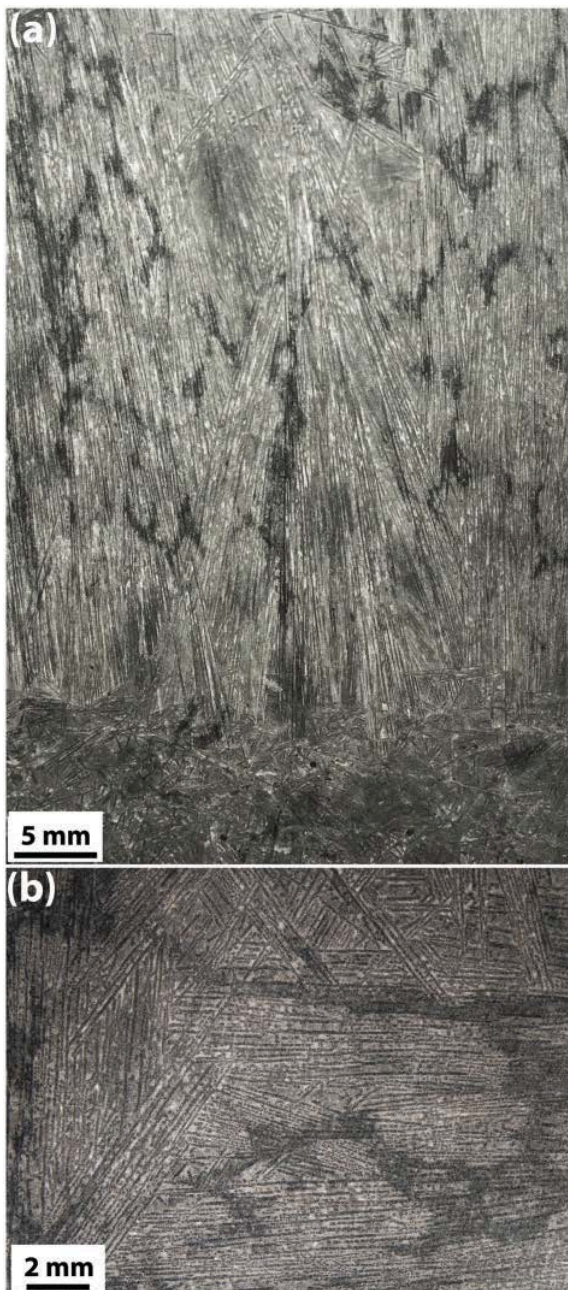
Fig. 11. Photographs of orthogonal sections through A3 Zone oriented platy pyroxene spinifex from type section at Locality 1 (Fig. 4; 649896mE, 7032746mN GDA94/MGA Z50). (a) Interface between A3 Zone oriented platy spinifex and A4 Zone acicular pyroxene (section cut parallel to profile; i.e. x–z or y–z); (b) oriented platy spinifex cut perpendicular to profile (x–y section) showing obliquely oriented plate sets.

intersection. The largest of the first-order plates extend beyond the volume that was imaged, and we report only minimum lengths and/or widths for these plates (>6610 μm and >5850 μm, respectively). The thicknesses of these plates are well constrained and measurements vary from

95 to 165 μm. First-order plates are locally limited in one or more directions by the crystal faces of other first-order plates. In some instances, plates develop acicular protrusions on their edges, particularly where they protrude into glassier domains of the sample. Acicular protrusions from the plate margin are shown for the 3D digitized crystal in Fig. 17c. Parallel stacked plates (in a plate set) also locally show a transition to domains of similarly aligned, acicular crystals (see Videos 1 and 2 in Supplementary Data Electronic Appendix 1). Figure 17d shows an example of a plate to acicular crystal transition in a first-order plate set; six acicular crystals can be
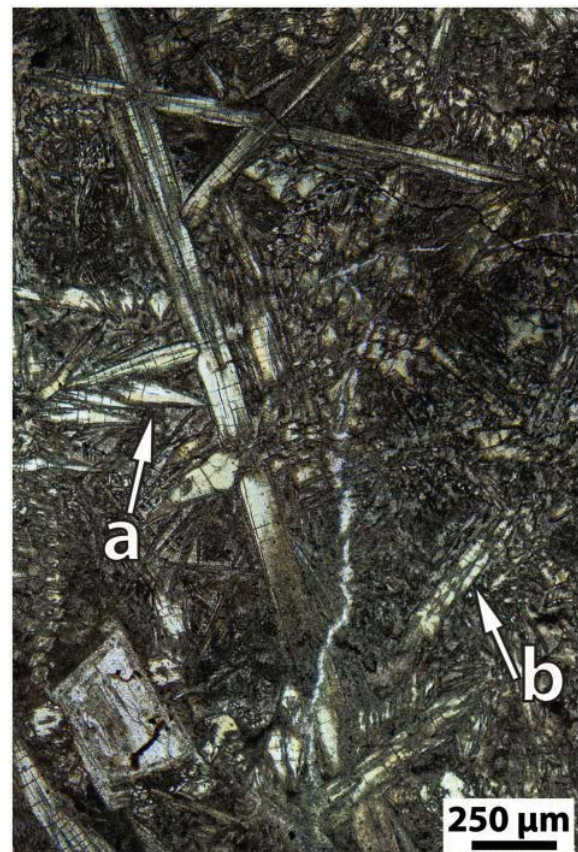
Fig. 12. Photomicrograph (PPL) of A_4 Zone at Locality 1 (649896mE, 7032746mN GDA94/MGA Z50) composed predominantly of (a) acicular zoned clinopyroxene phenocrysts in a fine-grained matrix, and locally (b) skeletal zoned pyroxene phenocrysts that resemble plates from the $_{A2–3}$ Zone.

observed in the same plane of the adjacent plate, and these are oriented in one direction, parallel to the crystallographic c-axis, and in crystallographic continuity.
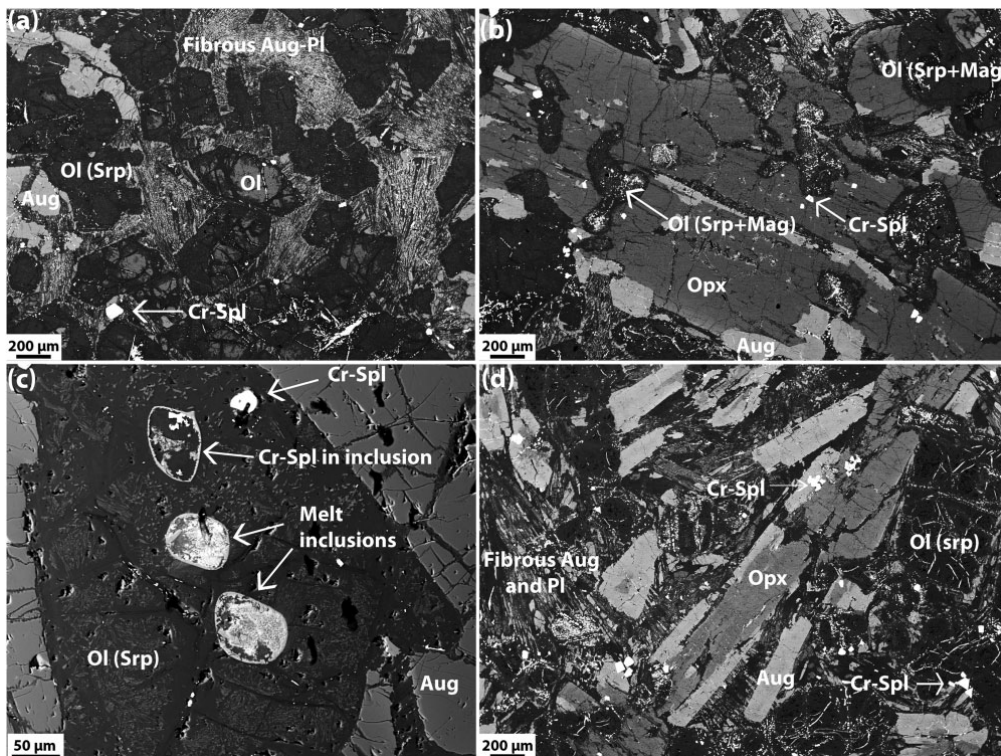
Fig. 13. BSE images of B2 Zone cumulate. (a) Relict olivine in serpentinized polyhedral phenocrysts. Matrix comprises fibrous dendrites of plagioclase and augite. White euhedral phenocrysts are Cr-spinel; lighter oikocrysts surrounding olivine (top left) are augite (sample 209122). (b) Poikilitic orthopyroxene (Opx), augite and serpentine after olivine, with some relict olivine. Poikilitic habit pyroxene encloses only subhedral olivine, suggesting it came before olivine formed euhedral crystal habits. Olivine locally encloses euhedral Cr-spinel and hence must have crystallized after Cr-spinel (sample 209122). (c) Olivine locally contains melt inclusions that are typically strongly altered. The inclusions, in turn, locally contain fine, euhedral Cr-spinel microphenocrysts (sample 209122). (d) Coarsely branching pyroxene (compared with A2–3 Zone) (sample 209116). In images (a), (b) and (d) the cumulate crystals are set in a matrix with a distinctly fibrous texture. The darker regions of this fibrous matrix are plagioclase whereas lighter regions are augite.

Second-order plates do not crosscut first-order plates; they typically form discrete plates that are con-fined within the interstitial spaces between oblique first-order plate sets (Fig. 17e and f). Second-order plates are typically much smaller than first-order plates in all dimensions, with length 190–1460 μm, width 100–710 μm, and thickness 30–70 μm. These relationships indicate that first-order sets crystallized before second-order sets. Second-order plates have the same X-ray intensities as the rims of first-order plates and are similar in composition (see 'Mineral chemistry').

Discrete acicular pyroxene crystals occur throughout the volume, but in greater abundance in glassier domains. As with plates, acicular crystals typically terminate abruptly where they meet obliquely oriented plates. They are typically oriented subparallel to adjacent plate sets, and they are locally in crystallographic continuity, indicating that plates and acicular crystals grew in association with one another. There are examples of discrete acicular crystals associated with plates of both first- and second-order scales. Representative first-order acicular crystals range from 1240 to > 1700 μm long, whereas second-order acicular crystals range from 150 to 730 μm long. Width and thickness (which are approximately equal) range from 120 to 245 μm for first-order acicular crystals and from 50 to 55 μm for second-order acicular crystals.

In first-order sets, both plates and acicular crystals have rims of higher X-ray intensity that surround a core of lower intensity; these correlate to the augite rims, and for altered cores described above and analysed by EPMA (see 'Mineral chemistry'), the rims range in thick-ness from 15 to 25 μm. Second-order plates and acicular crystals are characterized by similarly high X-ray intensity values to first-order, augite plate rims, but do not have the lower X-ray intensity, altered cores.

Further interrogation of their features is limited by the resolution of the data; however, back-scattered electron (BSE) images of thin sections of the same sample show the second-order crystals to be skeletal. Representative measurements of the thickness of second-order crystals are ~30–70 μm, which is roughly equivalent to the aver-age combined thickness of two rims, in the case of first-order plates and acicular crystals.

MINERAL CHEMISTRY

Electron probe microanalysis (EPMA)
The following is a description of the chemical variation for minerals from the A_2 Zone (sample 209114), and B_2 Zone (sample 209122). Table 3 summarizes the average compositions obtained.

In sample 209114, plate rims have close to ideal pyroxene stoichiometry, augite compositions and oxide totals between 98.3 and 99.85 wt % (Fig. 18, Table 3). They have lower Mg-numbers (47–76, average 67) and compatible trace element contents of Cr_2O_3 and NiO (≤ 0.11 wt % and ≤ 0.07 wt %, respectively) compared with B_2 Zone augites (see below), but higher Al2O3 (4.0–15.5 wt %, average 7.5 wt %) and TiO2 (0.4–1.3wt %, average 0.9 wt %), which probably reflect the different crystallization rates in their respective zones. Coish & Taylor (1979) suggested that Al–Ti content is directly related to cooling rate, and that under high cooling rates crystal growth in preferred orientations exceeds the diffusion rate of Al and Ti away from growth surfaces; thus they are effectively trapped within the crystal structure. High Al–Ti in pyroxene has also been observed in other spinifex-textured flows (e.g. Arndt et al., 1977; Arndt & Fleet, 1979; Kareem, 2005; Barr et al., 2009; Bouquain et al., 2009), and in rapidly cooled boninites (e.g. Coish & Taylor, 1979; Natland, 1982; Ohnenstetter & Brown, 1992).
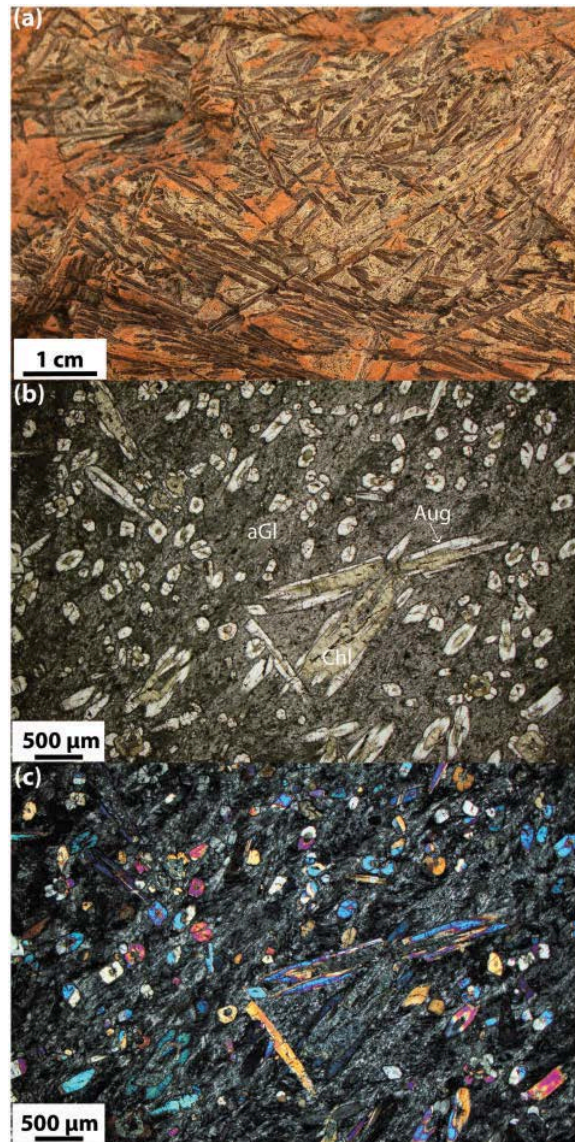
Fig. 14. Images showing random acicular pyroxene texture: (a) field photograph of hand sample at Locality 1 (650091mE, 7033593mN GDA94/MGA Z50); (b, c) photomicrographs from Locality 2 (652092mE, 7049072mN GDA94/MGA Z50). Zoned clinopyroxene phenocrysts are elongate in the direction of the crystallographic c-axis, with augite rims and chloritized cores (Chl). The cruciform twinned phenocryst in the centre right of the images should be noted. (b) PPL; (c) cross-polarized light (XPL).

Plate core material was analysed using a combination of EPMA point analyses and EPMA maps with mixed results (element maps and point analyses are included in Supplementary Data Electronic Appendix 2), probably because of the very fine grained, mixed nature of the alteration minerals. Variation diagrams of major element oxides for EPMA point analyses are

plotted in Fig. 19. They indicate that the alteration products are mostly a mixture of chlorite and quartz and potentially contain minor amounts of actinolite or weakly altered augite, but they do not appear to correlate with serpentine minerals, which typically have >40 wt % MgO (e.g. Deer et al., 2013). The average compositions are included in Table 3; they have large standard deviations, owing to the altered, heterogeneous nature of the mineralogy, but as an approximation they show the cores to contain high SiO_2, Al_2O_3, FeO (total Fe) and MgO, and low TiO_2, Cr_2O_3 and CaO. The plate cores have low oxide totals (90.8%), indicating that there has been a net loss of cations from them, which was presumably incurred during chloritization by the addition of H_2O. However, highly mobile elements such as K_2O and Na_2O are typically below detection levels and the FeO/MgO ratio is similar between the plate cores and rims (0.69 vs 0.79, respectively). Thus, we infer that cat-ion exchange was mostly restricted to within individual cores.
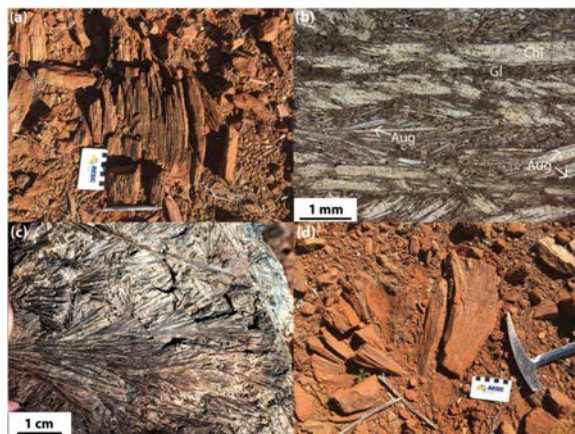
Fig. 15. Images of string-beef textured SHMB (sample 209115). (a) Field photograph of outcrop at Locality 1 (649744mE, 7032393mN GDA94/MGA Z50). (b) Photomicrograph (PPL) of thin section that is cut parallel to the long axis of the dominant crystal orientations. The zonation of clinopyroxene phenocrysts and the low volume of interstitial matrix material should be noted. (c)Coarsely branching morphology of acicular pyroxenes at Locality 1 (c. 649885mE/7032525mN GDA94/MGA Z50). (d) String-beef cone structure at Locality 1 (649811mE, 7032459mN GDA94/MGA Z50).

The main cations are Si, Al, Mg and Fe, in quantities that are indicative of pyroxene or
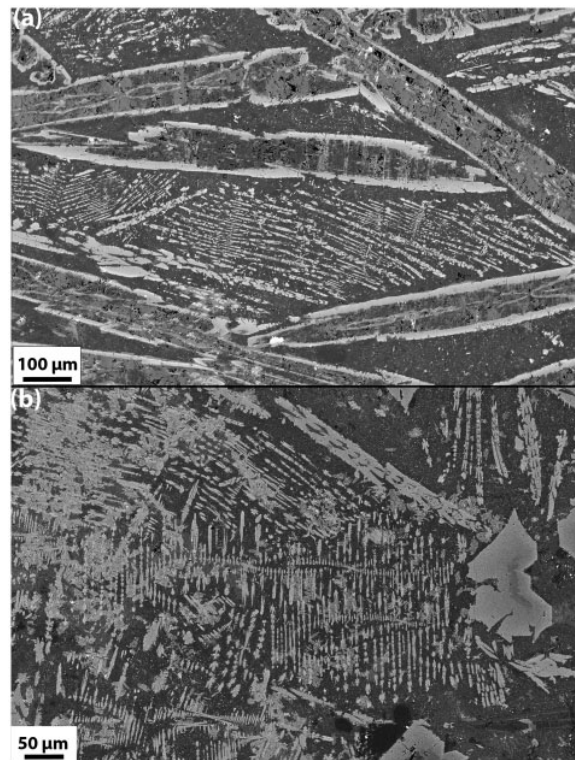
Fig. 16. BSE images of dendritic pyroxene forms: (a) A_2 Zone sample (209114; Locality 1). Dendrites occupy the space between first-order plates. It should be noted that dendrites have similar X-ray intensity to plate rims, and occur in sets of parallel chains or crystals. In three dimensions, these chains probably also define plates, but they are smaller than the resolution of our X-ray CT data. (b) Vitrophyric example from Locality 2 (within the Bassetts Volcanic Member; sample 221701). The similar morphology between skeletal crystals and dendrites, and the curvaceous central chains of several dendrites, should be noted.

amphibole chemistry. Figure 19 shows that plate core analyses overlap with the field for augite for the main cation elements except CaO; if plate cores have experienced a moderate net loss of CaO, then augite is a plausible precursor mineral. Similarly, if plate cores have experienced a moderate net loss of MgO then pigeonite is a plausible precursor mineral. Olivine is not considered a likely pre-cursor mineral, because Si and Al are too high, and MgO and Ni are too low. The closest amphibole composition is anthophyllite. Whereas we do not rule it out as a possible precursor, we could find no documented volcanic examples of anthophyllite. In contrast, zoned clinopyroxenes with pigeonite cores and augite rims are well documented in
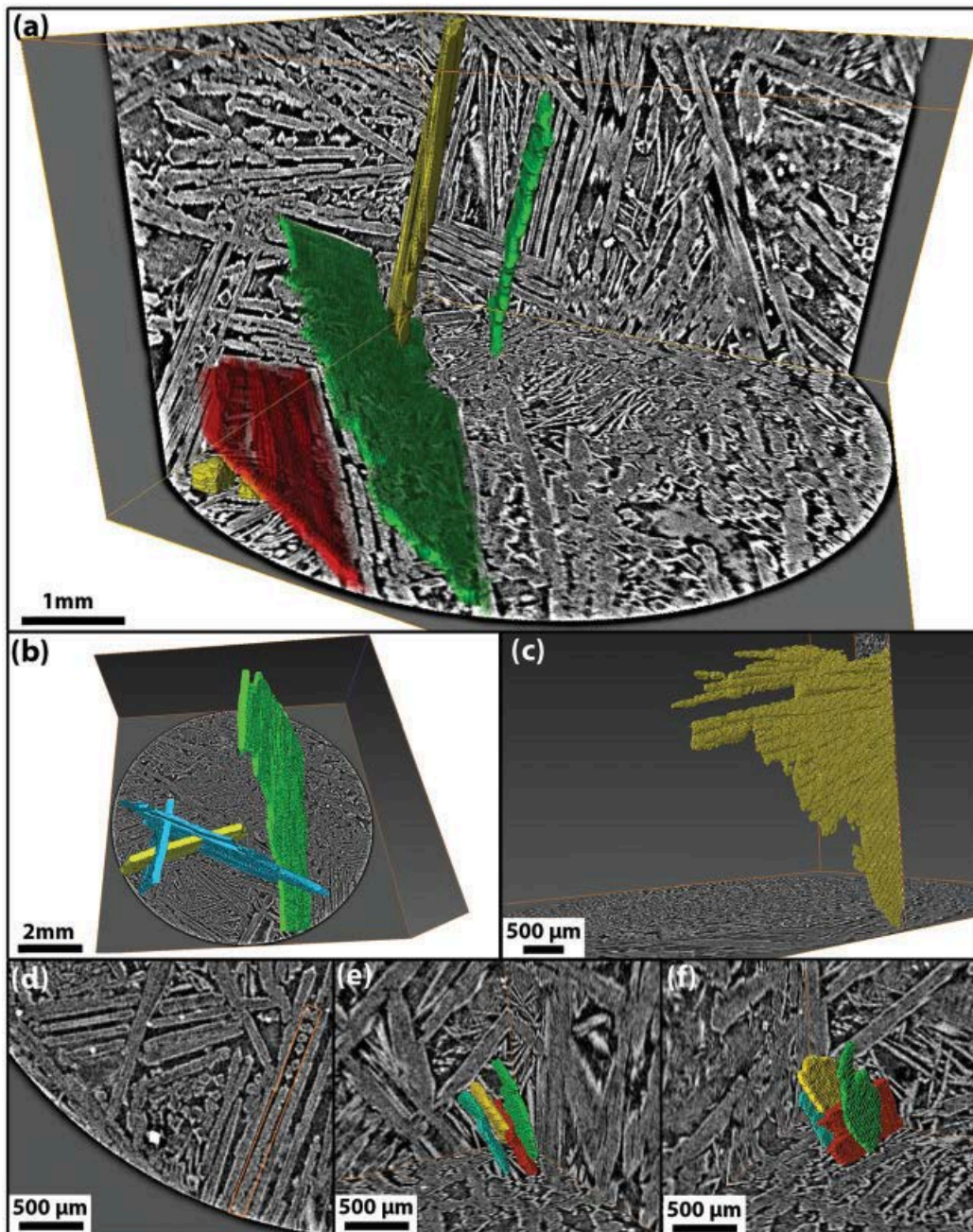
Fig. 17. Three-dimensional (3D) characterization of A2 Zone sample 209114. Background images have a B-spline background detection correction applied to remove background illumination; an Unsharp Masking filter was applied to sharpen the edges of features. Pixel intensity: pale grey, augite rim; mid grey, chloritized core; dark grey, devitrified glass; white, Cr-spinel. (a) Representative first order pyroxene crystals with platy aspect ratios; (b) first-order pyroxene crystals demonstrating intersecting relationships between obliquely oriented plates; (c) first-order pyroxene plate with acicular protrusions at one margin (this plate extends beyond the scanned volume); (d) acicular crystals oriented in the same plane as plate; (e) and (f) illustrate a second-order plate set viewed from slightly oblique directions (note that plates are truncated by first-order plates observable in the background image).

Archean komatiites and high-Mg basalts (e.g. Arndt et al., 1977; Puchtel et al., 1996; Stiegler et al., 2012), and in these rock types pigeonite alters to chlorite more readily than does augite (e.g. Arndt & Fleet, 1979). We have identified variably preserved pigeonite in the cores of zoned phenocrysts in the underlying Bassetts Volcanic Member. Those pigeonites had high-Al compositions (~3.6wt % Al_2O_3; sample 209130, Supplementary Data Electronic Appendix 2), and in examples where pigeonite cores were partially

altered, they have altered to similar chlorite-dominated assemblages.

Olivine compositions from the B_2 Zone range from $Fo_{88.2}$ to $Fo_{89.6}$ and average $Fo_{89.1}$. NiO in olivine ranges from 0.37 to 0.41 wt % and Cr_2O_3 from 0.1 to 0.25 wt %.
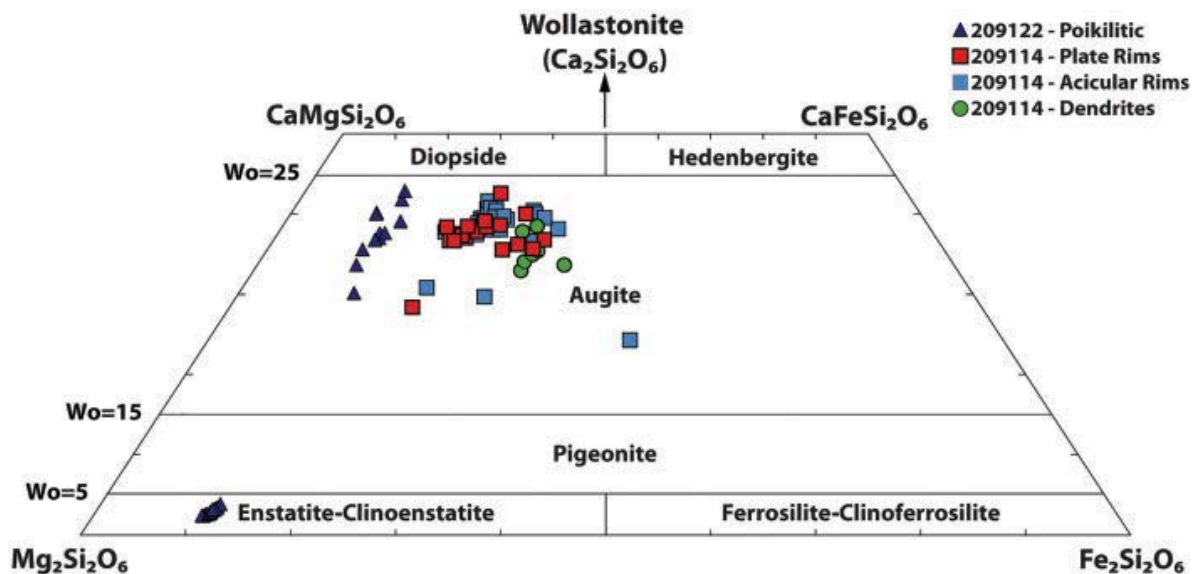
Fig. 18. Pyroxene quadrilateral diagram (after Morimoto et al., 1988). The 209114 plate cores are all altered.

All B_2 Zone pyroxene analyses are from poikilitic crystals. They form a trend on the pyroxene quadrilateral diagram that is relatively straight, although discontinuous through the miscibility gap, with both orthopyroxene and augite compositions (Fig. 18, Table 3). Compared with A_2 Zone augites, B_2 Zone augites have higher Mg-numbers (82–86, average 85) and higher concentrations of the compatible trace elements Cr_2O_3 and NiO (0.09–0.11 wt % and 0.11–0.79 wt %, respectively), but lower concentrations of Al2O3 (1.7–4.8 wt %, average 3.4 wt %) and TiO_2 (0.25–0.7wt %, average 0.45 wt %). Orthopyroxenes have high Mg-numbers (88–89) and high concentrations of compatible Cr_2O_3 (0.41–0.68 wt %, average 0.56 wt %) and NiO (0.13–0.17 wt %, average 0.15 wt %), and very low concentrations of the incompatible elements Al_2O_3 (0.5–1.4 wt %, average 1.0 wt %) and TiO_2 (0.08–0.15 wt %, average 0.11 wt %). The average composition of ortho-pyroxene is $En_{86.2}Fs_{10.9}Wo_{2.9}$, classifying it as enstatite after the Morimoto et al. (1988) scheme.

Stoichiometry for olivine is close to ideal, with a total of 2.99 cations per 4 oxygens, including 1.01 Si cations. As expected, average concentrations of the incompatible elements Al_2O_3 and TiO_2 are very low (0.06 wt % and 0.01 wt % respectively). Olivine was not found in the A_2 Zone.

The ferric iron content of Cr-spinel has been calculated using the method of Barnes & Roeder (2001). Ratios of $Fe^{3+}/(Cr + Al + Fe^{3+})$ are exceptionally low when compared with global datasets of terrestrial spinel compositions (e.g. Barnes & Roeder, 2001), aver-aging 0.08 and 0.09 for A_2 and B_2 Zone Cr-spinels respectively. Ratios of $Cr/(Cr þ Al)$ are exceptionally high, with averages of 0.89 for both A_2 and B_2 Zone Cr-spinels. Ratios of $Fe^{2+}/(Fe^{2+} + Mg)$ are also relatively high at 0.41 and 0.30 for A_2 and B_2 Zone Cr-spinels, respectively. Barnes & Roeder (2001) presented two diagrams for discriminating between various terrestrial volcanic settings: $Cr/(Cr + Al)$ vs $Fe^{2+}/(Fe2^{2+} + Mg)$ and $Fe^{3+}/(Cr + Al + Fe^{3+})$vs $Fe^{2+}/(Fe2^{2+} + Mg)$. Cr-spinels from Locality 1 plot on, or close to, the p90 contours for komatiite for

both discrimination diagrams; however, they also border the p90 contours for both boninite and island arc basalts, erring to lower $Fe^{2+}/(Fe^{2+} + Mg)$ values among the latter two populations.

Two samples from the A_1 Zone (209118 and 221722) are fine-grained chilled flow tops that we interpret as representative of initial liquid compositions (Table 4). These rocks have compositions between those of
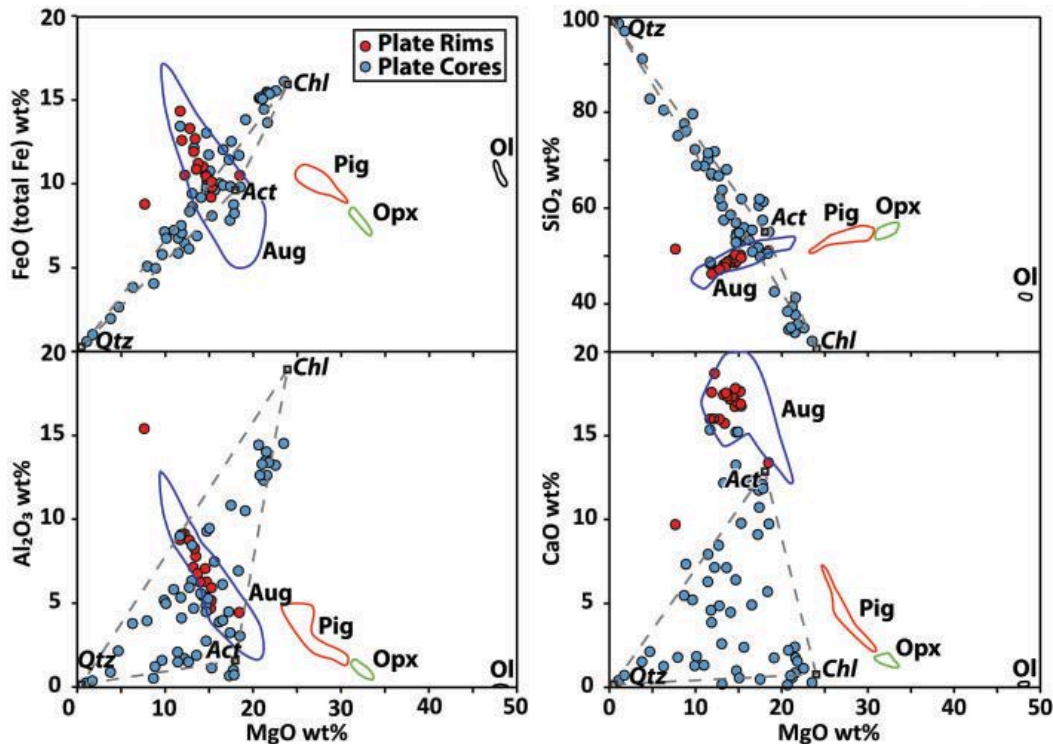

Fig. 19. Major element variation diagrams for EPMA point analyses collected in traverses across platy crystals in sample 209114. Black open squares give likely metamorphic alteration mineral compositions and grey dashed lines are tie lines between these compositions; Chl, Chlorite analysis 30 from Deer et al. (1962, table 25); Act, actinolite analysis 6 from Deer et al. (2013, table 23); Qtz, quartz (100% SiO_2). Outlined fields are EPMA composition ranges for fresh pyroxene and relict olivine in Meekatharra Formation samples from the Polelle Syncline analysed using similar operating conditions and standards.

WHOLE-ROCK CHEMISTRY

Geochemical variation is discussed with emphasis on elements considered immobile (e.g. major elements, Cr and Ni). Whole-rock chemical analyses for 19 samples collected from Locality 1 (Fig. 2) are reported in Table 4, including 18 volcanic rocks and one sedimentary rock from below the footwall contact. LOI values are ≤4.4wt% for non-cumulate rocks (low to moderate for Archean greenstones), and ~7 wt % for orthocumulates, reflecting hydration in association with the serpentinization process. Variation diagrams for MgO vs Al_2O_3, CaO, TiO_2, SiO_2, Cr and Ni are presented in Fig. 20 and MgO vs FeO (total Fe as Fe^{2+}) in Fig. 21.

the A_2 and B_2 Zone samples (Figs 21 and 22), because of olivine fractionation and accumulation in those zones respectively. They contain 51 and 52 wt % SiO_2, 15.8 and 14.4 wt % MgO, and their Mg-numbers are 73 and 71, respectively. They both contain 9 wt % Al_2O_3 and 0.6 wt % TiO_2, with $Al2O3/TiO2$ ratios of 14.6 (i.e. moderately Al-depleted relative to chondrite).

The string-beef sample and three A2 Zone samples have compositions ranging from 53 to 57 wt % SiO_2 and from 14.3 to 14.8 wt % MgO, and Mg-numbers from 68 to 74. They contain abundant zoned clinopyroxene (>90% in the case of the string-beef sample), and have fractionated a small amount of olivine; thus, they are probably enriched in SiO2 and slightly depleted in MgO relative to the initial liquid
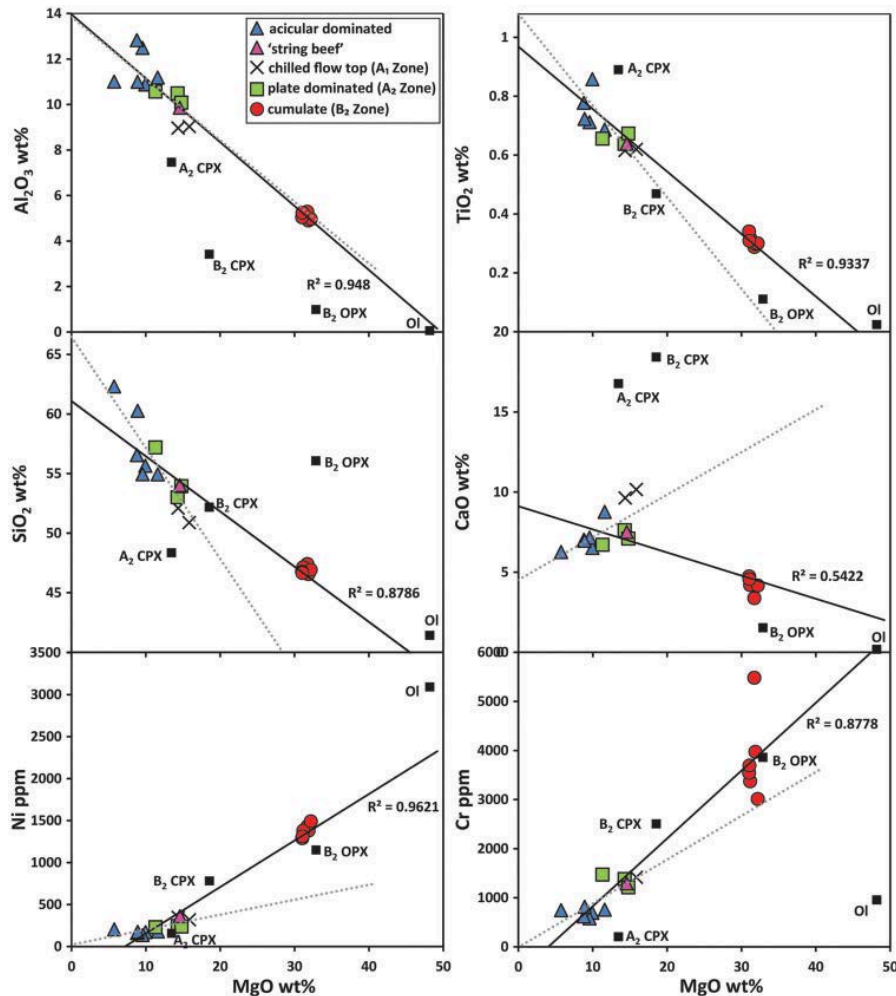
Fig. 20. Major element (anhydrous and normalized to 100%) variation diagrams for whole-rock analyses of 18 volcanic samples from Locality 1. Continuous line is a regression line for all samples in the cogenetic SHMB suite; dotted grey line is a regression curve for non-cumulate samples. Black squares are averages of measured compositions for A_2 Zone augite and B_2 Zone olivine, poikilitic Opx, poikilitic augite from EPMA analyses. Regression lines for MgO vs Al_2O_3, TiO_2, and Ni show strong correlations ($R^2 \geq 0.93$) and project close to the measured compositions of olivine in the B_2 Zone (sample 209122), demonstrating olivine control for these elements. In contrast, MgO vs SiO_2 and Cr show only moderate correlations ($R^2 = 0.88$ and 0.,88 respectively), which implies a more complex mineralogical control; probably pyroxene and Cr-spinel, respectively. CaO vs MgO has a poor correlation ($R^2 = 0.54$); this may reflect post-emplacement CaO mobility, or else possibly a more complex mineralogical control.

compositions. Al_2O has a narrow range from 9.9 to 10.6 wt % and TiO_2 is consistently around 0.65 wt %, with Al_2O_3/TiO_2 in these samples ranging from 15 to 16.5. Campbell & Arndt (1982) suggested that spinifex-textured rocks such as these contain cumulus pyroxene crystals and can be regarded as pyroxene cumulates; therefore they do not reflect frozen liquid compositions.

All six B_2 Zone samples are olivine–orthopyroxene–augite–Cr-spinel orthocumulates. They have homogeneous compositions, with SiO_2 consistently at 47 wt %and MgO ranging narrowly from 31 to

32.2 wt %. Mg-numbers range from 85 to 86, Al_2O_3 from 3.9 to 4.2wt % and TiO_2 is consistently ~0.3 wt %, with Al_2O_3/TiO_2 ranging from 14.8 to 18.4. B_2 Zone samples plot distinctly lower for SiO_2 and TiO_2, and higher for Ni than would be expected by simply extrapolating along the non-cumulate regression line (dashed line in Fig. 20), which is probably due to a combination of fractionation or accumulation of olivine and pyroxene and mobility of MgO and other elements during alteration. Within the B_2 Zone samples, there is a large spread in Cr abundance, ranging from 3010 to 5480 ppm, which produces a near-vertical

trend in this subpopulation in the MgO vs Cr diagram (Fig. 20), indicating Cr-spinel accumulation.

The six vitrophyric basalt samples from above the spinifex-textured sequence (Fig. 2) range from 55 to 62 wt % SiO_2 and from 5.6 to 11.7 wt % MgO. They contain 10.9–12.8 wt % Al_2O_3 and 0.7–1.0 wt % TiO_2, with Al_2O_3/TiO_2 ratios of 10.9–17.5 (i.e. strongly Al-depleted to relatively Al-undepleted). Because the samples are mostly fine grained, we do not consider them to have accumulated significant pyroxene, like the underlying spinifex-textured rocks. The compositions of vitrophyric-textured rocks are therefore representative of their respective liquids, which are notably more siliceous and less magnesian than the composition that we have inferred for the spinifex-textured rocks from A1zone chilled margins.
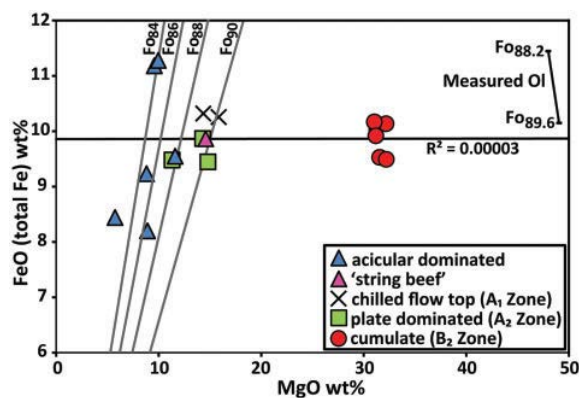
Fig. 21. FeO (total Fe) wt % vs MgO wt % (anhydrous and normalized to 100%) (after Barnes, 2006). Symbols are the same as for Fig. 20, but the range of Fo values for olivine EPMA analyses (from sample 209122, B2 Zone cumulate) is shown rather than the average. Continuous grey diagonal lines represent FeO/MgO ratios of liquids in equilibrium with a particular olivine Fo content, as calculated by the equation: $K_D=(FeO/MgO)_{Ol} \times (FeO/MgO)_{liquid} =0.3$ (after Roeder & Emslie, 1970, at 0_1 MPa). There is good agreement between the calculated FeO/MgO ratio for melts in equilibrium with the measured olivine compositions ($Fo_{88.2–89.6}$) from sample 209122 and the FeO/MgO ratio for the chilled upper margin samples (in equilibrium with $Fo_{90.2}$).

In Fig. 21 it is demonstrated that chilled liquid, platy pyroxene and string-beef samples plot on or close to FeO/MgO ratios

that are in equilibrium with olivine of Fo88–90 composition, which approximates the measured olivine compositions from B2 zone sample 209122. In comparison, vitrophyric basalts have higher FeO/MgO ratios and their liquid compositions would have been in equilibrium with less magnesian olivine (Fo84–88), indicating that their liquid compositions have fractionated olivine and pyroxene.

Although the samples from Locality 1 are relatively unaltered compared with most Archean greenstones, the different sample groups show variable enrichment in mobile incompatible elements (e.g. Cs, Rb, Ba; Fig. 22), which is probably alteration related. In contrast, the relatively immobile incompatible elements [e.g. Th, Nb, Zr, Hf, and rare earth elements (REE)] increase in abundance systematically with MgO, indicating olivine control; the different portions of the flow have identical shaped mantle-normalized multi-element patterns (Fig. 22). The significant feature of all the patterns is the light REE (LREE) enrichment between Sm and La, with relatively flat middle to heavy REE (MREE to HREE) patterns between Gd to Lu. All samples have a small negative Eu-anomaly. The analysis of the footwall felsic volcaniclastic sample also has similarly elevated incompatible elements, much higher LREE, but mostly flat HREE, with a slight kick between Er and Lu that may be attributed to minor amphibole fractionation, or may be within analytical error of a flat HREE pattern.

SPINIFEX TEXTURES

In our study area, we observe that spinifex textures and internal flow differentiation can occur over a broad range of chemical compositions from komatiite to andesite. In a review of spinifex textures in the literature, we also found reports of spinifex textures in volcanic rocks with extreme compositions. In the Musgraves Province of Western Australia, Howard et al. (2011, fig.

7a) have reported platy calcic amphibole spinifex in rhyolite, and, in southwestern Namibia, Cooper & Reid (1991) have reported platy calcite spinifex in a carbonatite flow. In the latter example, the flow was similarly differentiated into an upper spinifex horizon and a lower dolomite cumulate layer. Unlike pyroxene spinifex, those examples are unlikely to be mistaken for being komatiite, but they demonstrate that spinifex textures occur over a broad compositional spectrum.

Western Australia (Sun et al., 1989; Arndt et al., 2001) and from Proterozoic flows at Gilmour Island in Hudson Bay in Canada (Arndt, 1982) and the Lion Hills in the SE Baltic Shield in Russia (Puchtel et al., 1996).

In the above examples, pyroxene is the dominant phase in spinifex zones and it has typically been reported in variations of acicular habits. However, some notable exceptions do exist, as follows.
1. Viljoen & Viljoen (1969) documented platy pyroxene pseudomorphs that are enclosed between large randomly oriented
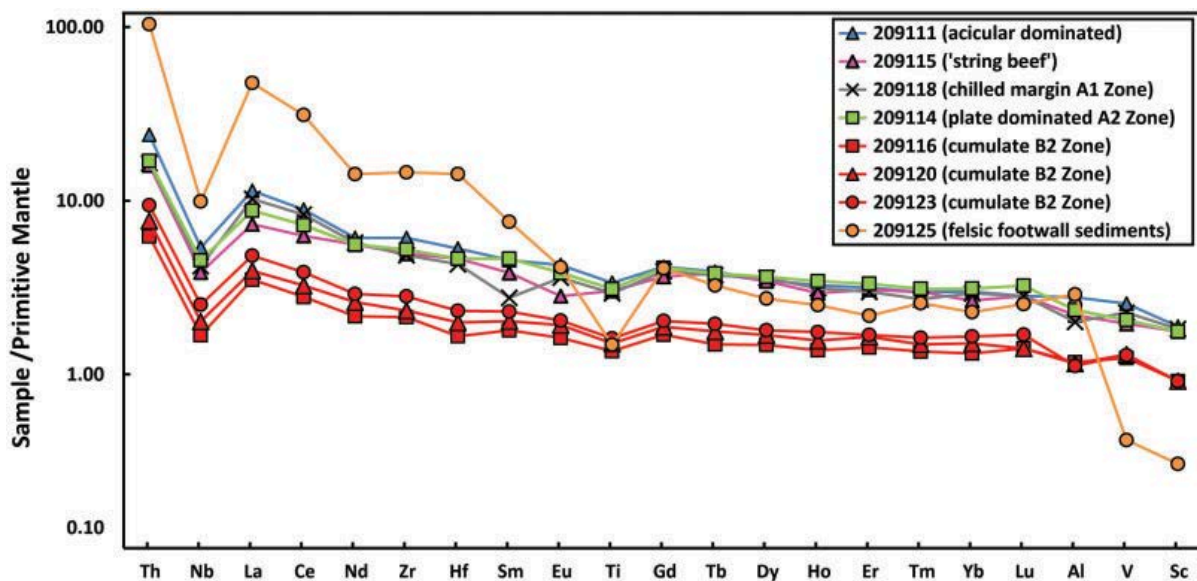
Fig. 22. Multi-element plot of representative samples normalized to primitive mantle [normalizing values after Palme & O'Neill (2014)].

Comparison with other pyroxene spinifex-textured sequences
Pyroxene spinifex in the upper parts of differentiated flows has been well documented in Archean komatiitic sequences in Canada (Arndt et al., 1977; Barnes, 1985), South Africa (Wilson & Versfeld, 1994; Wilson, 2003; Kareem, 2005; Stiegler et al., 2012) and Zimbabwe (Bickle et al., 1993; Orpen et al., 1993; Renner et al., 1994; Shimizu et al., 2005). Variations of pyroxene spinifex are also common in flow tops in Archean basalt sequences that do not have an obvious komatiite (sensu stricto) composition in the Mallina Basin of the Pilbara Craton in

olivine plates (their 'crystalline quench structures') from the Komati Formation in the Barberton Greenstone Belt in South Africa.
2. Wilson & Versfeld (1994) reported platy spinifex textures from the Nondweni Greenstone Belt in South Africa, which they suggested may have been igneous amphibole.
3. Renner et al. (1994) included descriptions of 'chain augite' from Zimbabwe, but although they have a similar appearance in 2D sections to our platy examples, it is unclear whether those crystals are also elongate in a second dimension and therefore platy.

4. Wood (1980, fig. 1b) documented platy pigeonite pseudomorphs (now chlorite) with augite rims in a boninite from the Kopi Formation in New Zealand.
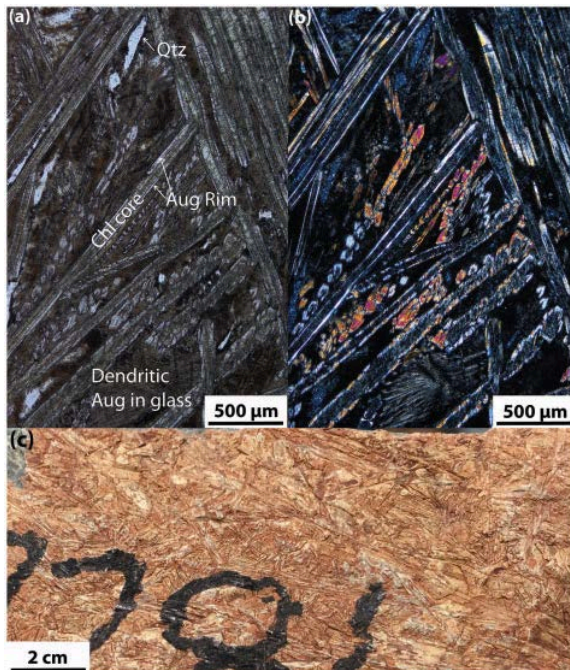

Fig. 23. Images of platy pyroxene spinifex texture from Pilbara Craton SHMB [sample 142281, collected by Smithies et al. (2004)]. (a) Photomicrograph taken in PPL (Chl core, chlorite core; Aug, augite; Qtz, quartz); (b) photomicrograph of same view in CPL; (c) photograph of hand sample (field of view 5cm wide).

We present the first documented example of platy pyroxene from the Yilgarn Craton, but this texture is not unique to our study area. When we identified this new texture within the Youanmi Terrane, we broadened our search within Western Australia and identified similar platy pyroxenes in the Louden Volcanics from the Mallina Basin in the Pilbara Craton (Fig. 23a–c). Other examples may also have been misrepresented in the literature, owing to entrenched ideas about platy olivine and acicular pyroxene, and the limitations of traditional 2D petrography.

In high-Mg basalts near Kambalda in Western Australia, there appears to be confusion about the phase that constitutes the platy crystals; in the study by Said & Kerrich (2010), their fig. 3e caption refers to platy pyroxene, whereas the discussion refers to it as platy olivine.

In other examples, photomicrographs show zoned clinopyroxene crystals that are all in parallel alignment, but they have been interpreted as being acicular crystals that have all been cut perpendicular to the c-axis (e.g. Orpen et al., 1993, figs 4.6p, 4.6r and 4.7a; Bouquain et al., 2009, samples Ax105 and M626 on p602). Considering our study, platy spinifex rocks, especially those with high SiO_2, might benefit from a reassessment of their petrography to confirm the platy phase. Pyroxene spinifex rocks with parallel crystal growth, like the examples above, might also benefit from 3D petrography to confirm the crystal morphology.

Development of platy pyroxene

Because this is the first documented example of platy pyroxene, in nature or the laboratory, any discussion surrounding preferential growth of plates instead of the more typical acicular forms must be speculative. To constrain this discussion, we refer to a combination of our observations from this type locality, and relate these to insights from experimental studies of similar textures.

In our study area, platy pyroxene and string-beef texture are developed only in samples that contain ~11–16 wt % MgO, with Mg-numbers $\geq$ 68. More generally, spinifex textures are restricted to high-Mg volcanic or subvolcanic rocks, such as komatiites and komatiitic basalts (e.g. Arndt et al., 2008), and it is intuitively reasonable to assume that moderate- to high-Mg liquid compositions are required to form these textures.

Flows with platy pyroxene are typically differentiated into an olivine-bearing cumulate basal layer and a spinifex-textured upper layer. In contrast, vitrophyric, trachytic or porphyritic flows, dominated by acicular pyroxene phenocrysts, are comparatively massive.

This is probably in part due to flow thickness; differentiated flows are thicker and cool over a wider range of thermal gradients. However, there could also be differences owing to eruption temperature and/or the amount of pyroxene phenocrysts already contained in the liquid prior to eruption.

been modified when grown in the presence of an 'impurity' (e.g. Buckley, 1949; Joshi, 2012). The modified platy pyroxene habit might have been influenced by the presence of an unknown habit-modifier in the silicate melt; this hypothesis could be explored in experimental studies.

Table 5: Compositions of selected komatiites and other high-MgO liquids (after Arndt, 2008), including Louden Volcanics analysis from 'chill zone' sample 96957 from Arndt et al. (2001)

	Commondale, South Africa	Barberton, South Africa	Alexo, Canada	Belingwe, Zimbabwe	Louden Volcanics, Australia	Bundle Volcanic Member (this study)
	High-Si komatiite	Al-depleted komatiite	Al-undepleted komatiite	Al-undepleted komatiite	SHMB	SHMB
SiO_2 wt %	49·9	46·8	45·9	49·4	54·2	50·9
TiO_2 wt %	0·11	0·38	0·35	0·41	0·42	0·62
Al_2O_3 wt %	7·6	4·43	7·1	8·66	10·54	9·03
FeO(tot) wt %	5·4	11·45	10·92	11·6	10·87	10·26
MnO wt %	0·12	0·18	0·17	0·1	0·19	0·2
MgO wt %	30·8	30·28	28·21	20	13·19	15·85
CaO wt %	5·4	5·78	6·57	8·6	8·28	10·16
Na_2O wt %	0·34	0·07	0·29	0·92	2·01	1·38
K_2O wt %	0·01	0·01	0·1	0·05	0·24	0·21
Volatile content	<0·5	<0·5	<0·5	<0·5	—	—
Max. Fo	96·3	93·9	94·1	91·3	~88*	89·6
Anhydrous liquidus °C	1616	1606	1564	1400	1290	1312–1342
Probable eruption temperature °C	~1600	~1600	~1550	1430	~1290	~1340

*Fo content calculated to be in equilibrium with liquid composition.

The skeletal nature of platy pyroxene indicates that it grew under high degrees of undercooling, and that crystal growth was rapid, similar to dendritic crystal growth (Faure et al., 2006). Indeed, first-order plates have dendrite-like interiors. Crystal growth may have initially been dendritic, prior to ripening, and in that case the initial dendrite shape would influence the final crystal habit. The nucleation of first-order plate cores and second-order augite plates was probably homogeneous, whereas augite overgrowths on first-order plates were probably heterogeneous, nucleating on the existing plate cores. In all cases, crystal growth was probably limited by the rate of diffusion between liquid and crystals (see discussions by Donaldson, 1979; Faure et al., 2006).

In crystal growth experiments in aqueous solutions, mineral habits have

Experimental study of spinifex texture
In the Faure et al. (2006) experimental study of olivine spinifex, they recreated vertically oriented plates of olivine (A3 Zone-like) under 'low' cooling rates (2–5° C h^{-1}) and 'normal' thermal gradients (~20° C cm^{-1}). They were also able to measure accurately the degree of undercooling during crystal growth, which for olivine was 37–56°C below the equilibrium liquidus. Oblique sections through those plates demonstrate apparent juxtaposition of olivine units (Faure et al., 2006, fig. 5b), which superficially resembles the juxtaposed acicular pyroxene crystals that we show in Fig. 8a and b. The observations from those experiments correspond well to spinifex textures from natural examples of olivine spinifex. We assume that similar cooling rate, thermal gradient, and degree of undercooling applied to flows in our example, given the similar vertical positions

of the A_2 and A_3 Zones. However, Faure et al. (2006) also ran cooling experiments with pyroxene-like compositions, keeping other variables similar, and the pyroxenes that crystallized appear to be long, hollow, acicular crystals, similar to those in string-beef texture (Table 1, Fig. 15a, b and d). Given the similarities between their pyroxene crystals in 2D sections (Faure et al., 2006, fig. 17) and our transitional acicular–platy pyroxene examples, the transition from acicular to platy habit may be unpredictable.

Future experimental work may try to recreate platy pyroxene spinifex textures. We would suggest using starting compositions that approximate the liquid com-positions from the Bundle Volcanic Member, or from the Louden Volcanics (Table 5). It would also be reason-able to experiment with a composition that approximates the platy pyroxene-textured samples (Table 4), which would be saturated in the chemical components necessary to recreate this texture. A 3D petrographic study of experimentally created textures, including examples such as the Faure et al. (2006) pyroxene crystals, would further quantify the texture, especially as their unaltered nature would be well suited to automatic segmentation methods (see the 'X-ray computed tomography' section).

PETROGENESIS

Melt composition

Interrogation of the extensive collection of Meekatharra Formation volcanic samples (n ¼ 164) in the Geological Survey of Western Australia (GSWA) state geochemical database shows that nearly all volcanic rocks contain $\leq$ 16 wt % MgO. The only exceptions are samples that contain abundant equant olivine phenocrysts, such as olivine–pyroxene cumulates and picrites (e.g. sample 183914, ~20 wt % MgO; Van Kranendonk et al., 2013). We have not identified any flows within the Meekatharra Formation to be komatiite (sensu stricto), either by having liquid compositions >18 wt % MgO or by having platy olivine spinifex textures. Ultramafic volcanic rocks within the underlying Norie Group have been interpreted as komatiite (e.g. Barley et al.,2000), but these are separated from the Meekatharra Formation by a thick sedimentary sequence and they are inferred to be >10 Myr older. Like earlier researchers (Watkins & Hickman, 1990; Pidgeon & Hallberg, 2000; Van Kranendonk et al., 2013), we interpret those units to be related to an earlier magmatic event.

In Table 5, we compare the composition of the Bundle Volcanic Member, the most spinifex-rich member of the Meekatharra Formation, with well-studied komatiitic associations such as those of the Abitibi (Canada), Belingwe (Zimbabwe), Commondale (South Africa) and Barberton (South Africa) greenstone belts. All those examples, except for Commondale, have associated komatiitic basalt flows, with 12–16 wt % MgO, like the Bundle Volcanic Member. We also include in Table 5 an estimated liquid composition for the Louden Volcanics (Arndt et al., 2001), which contains only komatiitic basalt compositions. If the estimated liquid compositions in Table 5 have not been modified significantly from their initial melt compositions (e.g. by fractional crystallization), then they must vary consider-ably in their melting conditions: temperature, pressure, melt fraction, or a combination of these.

Compared with komatiitic basalts from most of the localities mentioned above, the Bundle Volcanic Member is enriched in SiO_2 and incompatible trace elements, such as LREE, large ion lithophile elements (LILE) and high field strength elements (HFSE). The pre-dominance of pyroxene in the fine-grained volcanic rocks of the Meekatharra Formation and as a cumulus phase at the bases of those flows indicates that high

SiO_2, at least, was a primary feature of the melt composition.

Dry liquidus and mantle potential temperature

Arndt et al. (2008), after Nisbet (1982), assessed the results of cooling experiments conducted at 1 atm pres-sure and determined that the relationship between MgO and the dry liquidus temperature is linear, and that liquidus temperature ($T^{\circ}C$) = 1033 + 19.5 x MgO. Accordingly, the liquid compositions derived from chilled flow top samples 209118 (15.85 wt % MgO) and 221722 (14.35 wt % MgO) give calculated dry liquidus temperatures of $1342^{\circ}C$ and $1312^{\circ}C$, respectively.

Herzberg et al. (2010) showed that mantle potential temperature (Tp) is also intimately related to MgO, and can be calculated using the equation Tp ($^{\circ}C$) = 1463 + 12.74 x MgO – 2974/MgO. Using this expression, we calculate the mantle potential temperature for the Bundle Volcanic Member to be 1440–1480$^{\circ}C$. Given that all the Meekatharra Formation volcanic rocks contain less than 18 wt % MgO (except for those with appreciable olivine accumulation), the calculated mantle potential temperature for this period of magmatism is <1530$^{\circ}C$, which is comparable with secular thermal Earth models for ambient mantle (e.g. Korenaga, 2008).

Geodynamic implications

In our study area, Van Kranendonk et al. (2013) have attributed the melting event that produced the Norie and Polelle Group volcanic rocks to the impingement of a mantle plume beneath the Yilgarn Craton at c. 2825–2800 Ma; they suggested that the high-Si and incompatible element enriched characteristics of the Meekatharra Formation reflect assimilation–fractional crystallization (AFC) processes. Our observations are consistent with some aspects of this model: an open magmatic system in an intracontinental or near continental margin setting, which would be prone to AFC processes. The mantle potential temperatures calculated above do not necessitate, or refute, a mantle plume origin, so that aspect remains equivocal.

Boninite-like chemistry in the lower parts of the Meekatharra Formation (Wyman & Kerrich, 2012) and primary hydrous minerals in the contemporaneous Narndee Igneous Complex in the southern Murchison Domain further complicate the mantle plume–AFC model. Ivanic et al. (2015) suggested that the geochemical characteristics of the Narndee Igneous Complex, which also has a relatively high Mg content, and is SiO_2 and LREE enriched, could be related to a metasomatized mantle source, ambient crustal assimilation or subduction-related inputs. Considering these studies, a more detailed petrological study of the Meekatharra Formation and a critical evaluation of those models is required.

FUTURE WORK

A concerted effort is encouraged to reassess high-Mg volcanic sequences for additional occurrences of platy pyroxene. We suggest study focusing on spinifex-textured rocks with 10–18 wt % MgO and 50–55 wt %SiO_2, particularly those with platy minerals, for both chemical and 3D petrographic analysis.

Experimental studies, using the appropriate compositions, cooling rates and thermal gradients (e.g. Faure et al., 2006), could yield similar pyroxene morphologies to those documented here. We suggest starting compositions similar to the compositions of the A_1 and/or A_2 Zones from our Locality 1 (i.e. very close to pyroxene itself).

Further work is required to establish a strong petrogenetic model for the formation of these high-silica and moderately LILE-enriched rocks. In addition, a chemo-stratigraphic assessment of the

Polelle Syncline in the Yilgarn Craton is the subject of continuing research.

CONCLUSIONS

Platy pyroxene is reported here from two Archean cratons in Western Australia: at 2.8 Ga in the Yilgarn Craton and at 3.1 Ga in the Pilbara Craton. It probably also occurs in other greenstone terranes, where it may have been misidentified either as platy olivine or acicular pyroxene based on pre-existing assumptions. Furthermore, as Phanerozoic examples of platy pyroxene spinifex exist, the texture may be present through-out the geological record.

Careful petrographic evaluation is required to distinguish dominant mineral species from one another in spinifex-textured rocks. The inference of any precursor mineralogy in altered examples should not be based upon crystal habit alone; instead we recommend using a combination of texture and whole-rock chemistry (where it can be demonstrated that the composition is largely unaffected by alteration). We have highlighted reports of platy spinifex textures in rocks ranging in composition from komatiite to rhyolite, and even carbonatite.

In our example, pigeonite or augite probably formed first-order plate and needle cores, then augite crystallized as epitaxial rims on first-order crystals and formed discrete second-order plates and needles, and, lastly, third-order dendritic augite formed in the interstices prior to quenching of the remaining liquid to glass. Plate growth was clearly rapid, and indicates a high degree of undercooling. Liquid composition, eruption temperature (relative to the pyroxene liquidus), cooling rate and thermal gradient are all important variables required to form platy pyroxene spinifex texture.

SUPPLEMENTARY DATA
Supplementary Data for published Journal of Petrology paper located at:

https://academic.oup.com/petrology/article/58/9/1671/4575136#supplementary-data

REFERENCES

Armstrong, J. T. (1988). Quantitative analysis of silicate and oxide materials: comparison of Monte Carlo, ZAF, and phi-rho-z procedures. Microbeam Analysis, 239-246.

Arndt, N. T. (1977). Thick, layered peridotite–gabbro lava flows in Munro Township, Ontario. Canadian Journal of Earth Sciences 14, 2620-2637.

Arndt, N. T. (1982). Proterozoic spinifex-textured basalts of Gilmour Island, Hudson Bay. Geological Survey of Canada, Paper 83–1A, 137-142.

Arndt, N. T. (1986). Differentiation of komatiite flows. Journal of Petrology 27, 279-301.

Arndt, N. T., Bruzak, G. and Reischmann, T. (2001). The oldest continental and oceanic plateaus: geochemistry of basalts and komatiites of the Pilbara Craton, Australia. In: R. E. Ernst and Buchan, K. L. (eds.) Mantle plumes: their identification through time. Geological Society of America, Boulder Colorado. 359-387.

Arndt, N. T. and Fleet, M. E. (1979). Stable and metastable pyroxene crystallization in layered komatiite lava flows. American Mineralogist 64, 856-864.

Arndt, N. T., Lesher, C. M., Houlé, M. G., Lewin, E. and Lacaze, Y. (2004). Intrusion and crystallization of a spinifex-textured komatiite sill in Dundonald Township, Ontario. Journal of Petrology 45, 2555-2571.

Arndt, N. T., Lesher, C. M. and Barnes, S. J. (2008). Komatiite. Cambridge University Press, New York, USA.

Arndt, N. T., Naldrett, A. J. and Pyke, D. R. (1977). Komatiitic and iron-rich tholeiitic lavas of Munro Township, Northeast Ontario. Journal of Petrology 18, 319-369.

Baragar, W. R. A. and Scoates, R. F. J. (1987). Volcanic geochemistry of the northern segments of the Circum-Superior Belt of the Canadian Shield. In: Pharoah, T. C., Beckinsale, R. D., and Rickard, D. (eds.) Geochemistry and mineralization of Proterozoic volcanic suites: Geological Society, London, Special Publication No 33. London, UK, 113-131.

Barley, M. E., Kerrich, R., Reudavy, I. and Xie, Q. (2000). Late Archaean Ti-rich, Al-depleted komatiites and komatiitic volcaniclastic rocks from the Murchison Terrane in Western Australia. Australian Journal of Earth Sciences 47, 873-883.

Barnes, S.-J. (1985). The petrography and geochemistry of komatiite flows from the Abitibi Greenstone Belt and a model for their formation. Lithos 18, 241-270.

Barnes, S. J. (2006). Komatiites: petrology, volcanology, metamorphism and geochemistry. In: S. J. Barnes (ed) Nickel deposits of the Yilgarn Craton: geology, geochemistry and geophysics applied to exploration. Society of Economic Geologists. 13-49.

Barnes, S. J. and Roeder, P. L. (2001). The range of spinel compositions in terrestrial mafic and ultramafic rocks. Journal of Petrology 42, 2279–2302.

Barr, J. A., Grove, T. L. and Wilson, A. H. (2009). Hydrous komatiites from Commondale, South Africa: an experimental study. Earth and Planetary Science Letters 284, 199-207.

Bickle, M. J., Arndt, N. T., Nisbet, E. G., Orpen, J. L., Martin, A., Keays, R. R. and Renner, R. (1993). Geochemistry of the igneous rocks of the Belingwe Greenstone Belt: alteration, contamination and petrogenesis. In: M. J. Bickle and Nisbet, E. G. (eds.) The geology of the Belingwe Greenstone Belt, Zimbabwe: A study of the evolution of Archaean continental

crust. Geological Society of Zimbabwe. 175-213.

Bloomer, S. H. and Hawkins, J. W. (1987). Petrology and geochemistry of boninite series volcanic rocks from the Mariana Trench. Contributions to Mineralogy and Petrology 97, 361-377.

Bouquain, S., Arndt, N. T., Hellebrand, E. and Faure, F. (2009). Crystallochemistry and origin of pyroxenes in komatiites. Contributions to Mineralogy and Petrology 158, 599-617.

Buckley, H. E. (1949). Habit modification in crystals as a result of the introduction of impurities during growth. Discussions of the Faraday Society 5, 243-254.

Campbell, I. H. and Arndt, N. T. (1982). Pyroxene accumulation in spinifex-textured rocks. Geological Magazine 119, 605-610.

Coish, R. A. and Taylor, L. A. (1979). The effects of cooling rate on texture and pyroxene chemistry in DSDP Leg 34 basalt: a microprobe study. Earth and Planetary Science Letters 42, 389-398.

Cooper, A. F. and Reid, D. L. (1991). Textural evidence for calcite carbonatite magmas, Dicker Willem, southwest Namibia. Geology 19, 1193.

Deer, W. A., Howie, R. A. and Zussman, J. (2013). An introduction to the rock forming minerals. The Mineralogical Society. London, UK.

Donaldson, C. H. (1976). An experimental investigation of olivine morphology. Contributions to Mineralogy and Petrology 57, 187-213.

Donaldson, C. H. (1979). An experimental investigation of the delay in nucleation of olivine in Mafic Magmas. Contributions to Mineralogy and Petrology 69, 21-32.

Donovan, J. J., Snyder, D. A. and Rivers, M. L. (1993). An improved interference correction for trace element analysis. Microbeam Analysis 2, 23-28.

Donovan, J. J. and Tingle, T. N. (1996). An Improved Mean Atomic Number Correction for Quantitative Microanalysis. Microscopy and Microanalysis 2, 1-7.

Emeleus, C. H. (1987). The Rhum layered complex, Inner Hebrides, Scotland. In: I. Parsons (eds) Origins of igneous layering. Springer. p. 263–286.

Faure, F., Trolliard, G., Nicollet, C. and Montel, J.-M. (2003). A developmental model of olivine morphology as a function of the cooling rate and the degree of undercooling. Contributions to Mineralogy and Petrology 145, 251-263.

Faure, F., Arndt, N. and Libourel, G. (2006). Formation of spinifex texture in komatiites: an experimental study. Journal of Petrology 47, 1591-1610.

Fowler, A. D., Berger, B., Shore, M., Jones, M. I. and Ropchan, J. (2002). Supercooled rocks: development and significance of varioles, spherulites, dendrites and spinifex in Archaean volcanic rocks, Abitibi Greenstone belt, Canada. Precambrian Research 115, 311-328

Hallberg, J. A. (2000). Notes to accompany the Hallberg Murchison 1:25 000 geology dataset 1989-1994. Geological Survey of Western Australia. Perth, Australia.

Herzberg, C., Condie, K. and Korenaga, J. (2010). Thermal history of the Earth and its petrological expression. Earth and Planetary Science Letters 292, 79-88.

Howard, H. M., Werner, M., Smithies, R. H., Evins, P. M., Kirkland, C. L., Kelsey, D. E., Hand, M., Collins, A., Pirajno, F., Wingate, M. T. D., Maier, W. D. and Raimondo, T. (2011). The geology of the West Musgrave Province and the Bentley Supergroup - a field guide. Geological Survey of Western Australia. Perth, Australia.

Ivanic, T. J., Nebel, O., Jourdan, F., Faure, K., Kirkland, C. L. and Belousova, E. A. (2015). Heterogeneously hydrated mantle beneath the late Archean Yilgarn Craton. Lithos 238, 76-85.

Joshi, S. S. (2012). Crystal habit modification using habit modifiers. In: N. Kolesnikov and Borisenko, E. (eds) Modern aspects of bulk crystal and thin film preparation. InTech. 618.

Kareem, K. (2005). Komatiites of the Weltevreden Formation, Barberton Greenstone Belt, South Africa: implications for the chemistry and temperature of the Archean mantle (Unpublished PhD Thesis). Department of Geology and Geophysics, Tulane University. Louisiana, USA.

Kareem, K. M. and Bryerly, G. R. (2003). Petrology and geochemistry of 3.3 Ga komatiites – Weltevreden Formation, Barberton Greenstone Belt (abstract). 34th Lunar and Planetary Science Convention, Lunar and Planetary Institute.

Kerr, A. C., Marriner, G. F., Arndt, N. T., Tamey, J., Nivia, A., Saunders, A. D. and Duncan, R. A. (1996). The Petrogenesis of Gorgona komatiites, picrites and basalts - new field, petrographic and geochemical constraints. Lithos 37, 245-260.

Korenaga, J. (2008). Urey ratio and the structure and evolution of Earth's mantle. Reviews of Geophysics 46.

Lofgren, G. E., Donaldson, C. H. and Usselman, T. M. (1975). Geology, petrology and crystallization of Apollo 15 quartz-normative basalts. Proceedings of the Sixth Lunar Science Conference79-99.

Morimoto, N., Fabries, J., Ferguson, A. K., Ginzburg, I. V., Ross, M., Seifert, F. A., Zussman, J., Aoki, K. and Gottardi, G. (1988). Nomenclature of pyroxenes. American Mineralogist 73, 1123-1133.

Natland, J. H. (1982). Crystal morphologies and pyroxene compositions in boninites and tholeiitic basalts from deep sea drilling project holes 458 and 459B in the Mariana fore-arc region. Initial reports of the Deep Sea Drilling Project 60, 681-707.

Nesbitt, R. W. (1971). Skeletal crystal forms in the ultramafic rocks of the Yilgarn Block, Western Australia: evidence for an Archaean ultramafic liquid. Geological Society of Australia Special Publication No. 3331-347.

Nisbet, E. G., Arndt, N. T. and Bickle, M. J. (1987). Uniquely fresh 2.7 Ga komatiites from the Belingwe greenstone belt, Zimbabwe. Geology 15, 1147-1150.

Ohnenstetter, D. and Brown, W. L. (1992). Overgrowth textures, disequilibrium zoning, and cooling history of a glassy four-pyroxene boninite dyke from New Caledonia. Journal of Petrology 33, 231-271.

Orpen, J. L., Martin, A., Bickle, M. J. and Nisbet, E. G. (1993). The Mtshingwe Group in the west: andesites, basalts, komatiites and sediments of the Hokonui, Bend and Koodoovale Formations. In: M. J. Bickle and Nisbet, E. G. (eds.) The geology of the Belingwe Greenstone Belt, Zimbabwe: A study of the evolution of Archaean continental crust. Geological Society of Zimbabwe. 69-86.

Pidgeon, R. T. and Hallberg, J. A. (2000). Age relationships in supracrustal sequences of the northern part of the Murchison Terrane, Archaean Yilgarn Craton, Western Australia: a combined field and zircon U–Pb study. Australian Journal of Earth Sciences 47, 153-165.

Puchtel, I. S., Hofmann, A. W., Mezger, K., Shchipansky, A. A., Kulikov, V. S. and Kulikova, V. V. (1996). Petrology of a 2.41 Ga remarkably fresh komatiitic basalt lava lake in Lion Hills, central Vetreny

Belt, Baltic Shield. Contributions to Mineralogy and Petrology 124, 273-290.

Pyke, D. R., Naldrett, A. J. and Eckstrand, O. R. (1973). Archean ultramafic flows in Munro Township, Ontario. Geological Society of America Bulletin 84, 955.

Renner, R., Nisbet, E. G., Cheadle, M. J., Arndt, N., Bickle, M. J. and Cameron, W. E. (1994). Komatiite Flows from the Reliance Formation, Belingwe Belt, Zimbabwe: I. Petrography and Mineralogy. Journal of Petrology 35, 361-400.

Roeder, P. L. and Emslie, R. F. (1970). Olivine-liquid equilibrium. Contributions to Mineralogy and Petrology 29, 275-289.

Said, N. and Kerrich, R. (2010). Elemental and Nd-isotope systematics of the Upper Basalt Unit, 2.7 Ga Kambalda Sequence: quantitative modelling of progressive crustal contamination of plume asthenosphere. Chemical Geology 273, 193-211.

Shimizu, K., Nakamura, E. and Maruyama, S. (2005). The geochemistry of ultramafic to mafic volcanics from the Belingwe Greenstone Belt, Zimbabwe: magmatism in an Archean continental large igneous province. Journal of Petrology 46, 2367-2394.

Stiegler, M. T., Cooper, M., Byerly, G. R. and Lowe, D. R. (2012). Geochemistry and petrology of komatiites of the Pioneer Ultramafic Complex of the 3.3 Ga Weltevreden Formation, Barberton Greenstone Belt, South Africa. Precambrian Research 212–213, 1-12.

Sun, S.-S., Nesbitt, R. W. and Mcculloch, M. T. (1989). Geochemistry and petrogenesis of Archaean and early Proterozoic siliceous high-magnesian basalts. In: A. J. Crawford (ed) Boninites. 148-173.

Taylor, R. N., Nesbitt, R. W., Vidal, P., Harmon, R. S., Auvray, B. and Croudace, I. W. (1994). Mineralogy, Chemistry, and Genesis of the Boninite Series Volcanics, Chichijima, Bonin Islands, Japan. Journal of Petrology 35, 577-617.

Van Kranendonk, M. J., Ivanic, T. J., Wingate, M. T. D., Kirkland, C. L. and Wyche, S. (2013). Long-lived, autochthonous development of the Archean Murchison Domain, and implications for Yilgarn Craton tectonics. Precambrian Research 229, 49-92.

Viljoen, M. J. and Viljoen, R. P. (1969). Evidence for the existence of a mobile extrusive peridotitic magma from the Komati Formation of the Onverwacht Group. Geological Society of South Africa, Special Publication No 2.

Watkins, K. P. and Hickman, A. H. (1990). Geological evolution and mineralization of the Murchison Province, Western Australia. Geological Survey of Western Australia. Perth. Australia.

Welsch, B., Faure, F., Famin, V., Baronnet, A. and Bachelery, P. (2013). Dendritic Crystallization: A Single Process for all the Textures of Olivine in Basalts? Journal of Petrology 54, 539-574.

Wilson, A. H. (2003). A new class of silica enriched, highly depleted komatiites in the southern Kaapvaal Craton, South Africa. Precambrian Research 127, 125-141.

Wilson, A. H. and Versfeld, J. A. (1994). The early Archaean Nondweni Greenstone Belt, southern Kaapvaal Craton, South Africa, Part II. Characteristics of the volcanic rocks and constraints on magma genesis. Precambrian Research 67, 277-320.

Wingate, M. T. D., Bodorkos, S. and Kirkland, C. L. (2008). 183921: felsic volcaniclastic rock, Lordy Bore; Geochronology Record 733. In: Compilation of geochronology data. Geological Survey of Western Australia.

Wood, C. P. (1980). Boninite at a continental margin. Nature 288, 692-694.

Wyche, S., Spagiari, C. V., Forbes, C. J., Bunting, J. A., Thebaud, N., Hollingsworth, D., Culpan, N. and Vearncome, J. (2007). A geological traverse across the northern Yilgarn Craton - a field guide. Geological Survey of Western Australia. Perth, Australia.

Wyman, D. A. and Kerrich, R. (2012). Geochemical and isotopic characteristics of Youanmi terrane volcanism: the role of mantle plumes and subduction tectonics in the western Yilgarn Craton. Australian Journal of Earth Sciences 59, 671-694.

Zhao, S.-R., Liu, R., Wang, Q.-Y., Xu, H.-J. and Fang, M. (2011). Skeletal morphologies and crystallographic orientations of olivine, diopside and plagioclase. Journal of Crystal Growth 318, 135-140.

Zhou, M.-F., Zhao, T.-P., Malpas, J. and Sun, M. (2000). Crustal-contaminated komatiitic basalts in Southern China: products of a Proterozoic mantle plume beneath the Yangtze Block. Precambrian Research 103, 175-189.